

IDENTIFYING GUT BACTERIA AND THEIR INTERACTIONS USING DEEP
LEARNING BASED IMAGE ANALYSIS AND GNOTOBIOTIC EXPERIMENTS

by

EDOUARD A. HAY

A DISSERTATION

Presented to the Department of Physics
and the Graduate School of the University of Oregon
in partial fulfillment of the requirements
for the degree of
Doctor of Philosophy

December 2019

DISSERTATION APPROVAL PAGE

Student: Edouard A. Hay

Title: Identifying Gut Bacteria and Their Interactions Using Deep Learning Based Image Analysis and Gnotobiotic Experiments

This dissertation has been accepted and approved in partial fulfillment of the requirements for the Doctor of Philosophy degree in the Department of Physics by:

Eric Corwin	Chair
Raghuveer Parthasarathy	Advisor
Staphanie Majewski	Core Member
Brendan Bohannon	Institutional Representative

and

Kate Mondloch	Interim Vice Provost and Dean of the Graduate School
---------------	--

Original approval signatures are on file with the University of Oregon Graduate School.

Degree awarded December 2019

© 2019 Edouard A. Hay
This work is licensed under a Creative Commons
Attribution-NonCommercial-NoDerivs (United States) License.



DISSERTATION ABSTRACT

Edouard A. Hay

Doctor of Philosophy

Department of Physics

December 2019

Title: Identifying Gut Bacteria and Their Interactions Using Deep Learning Based Image Analysis and Gnotobiotic Experiments

The microbial communities of animal intestines are composed of dozens to hundreds of species and play important roles in host development, health and disease. Due to the complexity of these communities, the determinants of the microbial composition, which may include physical characteristics or biochemical interactions, remain largely unknown. Understanding the spatial structure and the effect of bacterial interactions are paramount to learning more about how these communities are formed.

In this dissertation, we develop the use of a deep convolutional neural network for identification of individual bacteria in 3D images of the intestines of larval zebrafish which contain fluorescently labeled bacteria taken using light sheet fluorescent microscopy. This network achieves human expert level accuracy and we extend its use to multiple bacterial species through transfer learning. Next we show the application of U-net in segmentation of the intestine in phase contrast microscopy images. These two techniques can be used in the future to study the spatial structure of microbes in the zebrafish intestine.

Lastly, we present an experiment in which explore bacterial interactions within larval zebrafish. We consider commensal intestinal microbes in larval zebrafish, initially raised germ-free to allow introduction of controlled combinations of 1-5 bacterial species. Using dissection and plating assays, we find strong pairwise interactions between certain bacteria. In the 4 or 5 bacterial species communities, we find weaker interactions and a much higher than expected level of coexistence suggesting that the pairwise interactions are not sufficient to predict the composition of multispecies gut communities and that higher-order interactions may dampen strong competition.

This dissertation includes previously published and unpublished co-authored material.

CURRICULUM VITAE

NAME OF AUTHOR: Edouard A. Hay

GRADUATE AND UNDERGRADUATE SCHOOLS ATTENDED:

University of Oregon, Eugene, OR
Reed College, Portland, OR

DEGREES AWARDED:

Doctor of Philosophy, Physics, 2019, University of Oregon
Bachelor of Arts, Physics, 2011, Reed College

AREAS OF SPECIAL INTEREST:

Deep learning
Image processing
Host-microbe interactions
Winemaking

PROFESSIONAL EXPERIENCE:

Graduate Research Assistant, Parthasarathy Lab, University of Oregon,
Eugene, Oregon, 2015-2019
Graduate Teaching Fellow, University of Oregon, Eugene, Oregon, 2014-2016

GRANTS, AWARDS AND HONORS:

Incubating Interdisciplinary Initiative (I3) Award, University of Oregon, 2018.

PUBLICATIONS:

Taormina, Michael J., & Hay, Edouard A. & Parthasarathy, Raghuveer
(2017). Passive and active microrheology of the intestinal fluid of the larval
zebrafish. *Biophysical Journal*, Volume 113, Issue 4, 957-965.

Hay, EA. & Parthasarathy, R (2018). Performance of convolutional neural
networks for identification of bacteria in 3D microscopy datasets. *PLoS
Computational Biology*, 14(12): e1006628.

Wiles, Travis J. & Wall, Elena S. & Schlomann, Brandon H. Hay, Edouard A. & Parthasarathy, Raghuvver & Guillemin, Karen (2018). Modernized Tools for Streamlined Genetic Manipulation and Comparative Study of Wild and Diverse Proteobacterial Lineages. *mBio Journal*, 9(5): e01877-18.

Logan, SL & Dudley, C & Baker, RP & Taormina, MJ & Hay, EA & Parthasarathy, R (2018) Automated high-throughput light-sheet fluorescence microscopy of larval zebrafish. *PLOS ONE* 13(11): e0198705.

ACKNOWLEDGEMENTS

I would like to thank my entire family, immediate, extended, and married-in-to without whom I would never have become who I am today. Et particulièrement, mon grand-père, Claude Vaucher, parce que si tu ne manges pas du chocolat, tu meurs.

TABLE OF CONTENTS

Chapter	Page
I. INTRODUCTION	1
1.1. Preface	1
1.2. Imaging of Intestinal Microbiota in Larval Zebrafish	2
1.3. Deep Learning on Images	6
1.4. Interactions of Intestinal Microbial Communities	7
II. PERFORMANCE OF CONVOLUTIONAL NEURAL NETWORKS FOR IDENTIFICATION OF BACTERIA IN 3D MICROSCOPY DATASETS	10
2.1. Introduction	10
2.2. Results	15
2.3. Discussion	27
2.4. Future Directions	30
III. SEMANTIC SEGMENTATION	31
3.1. Introduction	31
3.2. U-net’s Architecture and Our Implementation	36
3.3. Results	38
3.4. Discussion	44

Chapter	Page
IV. MULTI-SPECIES MICROBIAL INTERACTIONS IN LARVAL ZEBRAFISH	45
4.1. Introduction	45
4.2. Methods	48
4.3. Results	49
4.4. Conclusions	57
REFERENCES CITED	59

LIST OF FIGURES

Figure		Page
1.1.	Schematic of a light sheet fluorescent microscope. A laser passes through an AOTF after which it is oscillated at a high frequency at a galvanometer (a), passes through a lens (b), then passes through a sample perpendicular to which is a camera that records the emitted light.	4
2.1.	Images of bacteria in the intestine of larval zebrafish. a) Schematic illustration of a larval zebrafish with the intestine highlighted in red. Scale bar: 0.5 mm. b) Single optical section from light sheet fluorescence microscopy of the anterior intestine of a larval zebrafish colonized by GFP expressing bacteria of the commensal <i>Vibrio</i> species ZWU0020. Scale bar: 50 microns. c) z, y and x projections from 28x28x8 pixel regions of representative individual <i>Vibrio</i> bacteria, d) non-bacterial noise, e) individual bacteria of the genus <i>Pseudomonas</i> , species ZWU0006, and f) autofluorescent zebrafish cells.	14
2.2.	Creation of the 3-D convolutional neural network. a) Agreement matrix between six individuals (members of the authors' research group), evaluated on a single dataset of images of <i>Vibrio</i> bacteria, and between those humans and the convolutional neural network. b) Accuracy vs number of kernels per layer using cross validation across the various imaging datasets, where the x-axis denotes the number of kernels in the first convolutional layer. The second convolutional layer for each plotted point has twice as many kernels as the first.	19
2.3.	Comparison of Convnet and feature based learning algorithms across all datasets. Comparison of accuracies for the various learning algorithms (convolutional neural network, support vector classifier, and random forest) across different <i>Vibrio</i> image datasets, as well as two image datasets from fish devoid of gut bacteria. Each accuracy was determined by training on the data from all of the other datasets, and testing on the dataset of interest.	22
2.4.	Data augmentation. Examining the accuracy of the CNN as a function of a) varying the training data size by adding images from biologically distinct datasets (New datasets) or by adding images randomly from the full set of images (Train/test split), and b) transformation of the data by image rotations and reflections	24

Figure	Page
2.5. Transfer learning on new bacterial sSpecies. The accuracy of Pseudomonas classification with convolutional neural networks trained in different ways. “Vibrio” indicates training on images of Vibrio bacteria, “Pseudomonas” indicates training on the small Pseudomonas image dataset, and “Transfer” indicates using the Vibrio-derived network weights as the starting point for training on Pseudomonas images. For training only on Vibrio images, the different data points come from random weight initialization, random data ordering, and random augmentation. For training only on Pseudomonas images, and for transfer learning, the different data points are from random train/test splits of the Pseudomonas data.	27
3.1. Pixel-by-pixel segmentation using convolutional neural network. Left is the input image with a window of width and height w at the center of which is the pixel to be classified. This window is passed through a convolutional neural network, center, which classifies the pixel as belonging to an object, in this example, gut or not-gut. . .	32
3.2. Example “fully convolutional network” used for segmentation. The image passes through a series of convolutional layers each followed by max pooling. After this, upsampling in the form of backwards convolution (deconvolution) is performed in series yielding a segmentation map.	33
3.3. Schematic of the U-net architecture. Similarly to the “fully convolutional network”, a series of convolutional layers and max pooling are performed followed by a series of up-convolutions. U-net also concatenates the contracting path to the expanding path.	35
3.4. DIC gut image with corresponding polygon mask. Example DIC image with polygon from Ryan Baker’s software. (A) labels a closed lumen, (B) labels interstitial fluid, (C) muscle tissue and (D) is a luminal opening containing a bacterial bolus. The scale bar is 100 μm	38
3.5. Example DIC gut images showing variable noise and quality. Each image is of a different fish. The scale bar is 100 μm	40
3.6. U-net segmentation on DIC gut images. DIC image followed by two different human’s masks and finally the predicted mask using U-net. The dice loss is given between the two human’s on the Human 1 mask panel. The dice losses between U-net and human 1 and human 2 are shown on the left and right respectively of each U-net image. The scale bars are 100 μm	42

- 3.7. **U-net segmentation on DIC gut images excluding lumen.** DIC image followed by two different human's masks and finally the predicted mask using U-net of the intestine excluding the lumen. The scale bars are $100 \mu\text{m}$ 43
- 4.1. **Image of larval zebrafish and bacterial species investigated.** (a) A 7 day post fertilization larval zebrafish; the dotted curve outlines the intestine. Scale bar: $500 \mu\text{m}$. (b) photograph of all five bacterial species plated on HiChrome universal agar on which all five species can be seen to grow to different colors and morphologies (c) Phylogenetic tree of the five bacterial species used in the experiment, also indicating the color scheme and abbreviations used throughout the text. Numbers indicate [whatever] metric of genetic distance. (d) The abundance per zebrafish gut of each of the five bacterial species when colonized in mono-association with the host, assessed as colony forming units (CFU) from plated gut contents. The violin plots indicate the distribution of CFU values, with the median and quartiles indicated by dashed lines, in $N = [35, 26, 18, 25, 25]$ fish (left to right). 48
- 4.2. **Pairwise bacterial interactions.** Split violin plots of the abundances per zebrafish gut of (a) AE and (b) EN in mono-association (left curve, repeated in each plot) and in di-association with each of the other bacterial species (right curve). Medians and quartiles are indicated by dashed lines. (c) Matrix of pairwise interaction coefficients determined from a linear additive model, described in the text. The mean and standard deviations as determined from bootstrap sampling are included. (d) The average total bacterial load in each of the di-association combinations, expressed as \log_{10} of total CFUs. The diagonal values are the mono-association load for each of the five species. 51
- 4.3. **Pairwise prediction of the five species community.** (a) Stacked bar plot of the relative abundance of the five bacterial species when all five were co-inoculated. Each bar is a single dissected fish and are ordered by total load. (b) Histogram of the total number of bacterial species from the 5-species inoculations. (c) Violin plots of the total load as a function of total number of inoculated species. (d) Prediction of the abundance of the five different bacterial species from the linear additive model compared to the actual abundance from the 5-species inoculations. 54
- 4.4. **4 and 5 bacterial species interactions.** (a) violin plot of the total abundance of EN in the 5-species experiment, left side, and each of the 4-species experiments, right side. (b) 4-5 species interaction coefficients.

Figure	Page
<p>The mean and standard deviation for each coefficient are included as determined from bootstrap sampling. (c) The 4-5 interactions plotted against the 1-2 interactions from Figure 2.</p>	57

CHAPTER I

INTRODUCTION

1.1. Preface

Microbial communities are found nearly everywhere on Earth; from within the rocks of the Atacama desert, to the ocean in which microbes make up 50-90% of the total biomass [1]. They are found within our intestines and stomach, and on our hair and skin. These microbes exist in structured communities called microbiomes that exist in ecological niches across wide ranging scales, from a few species to many thousands. A majority of these microbiomes are complex, heterogeneous communities across a broad diversity of taxa. This diversity is crucial to the stability of these biomes, much like is the case for the ecological communities of the old growth forests of the Pacific Northwest or other macro-ecological systems. There have been an unprecedented amount of imaging experiments on microorganisms in the past decade. This has led to a wealth of understanding of these creatures and has created image processing problems that defy conventional methods of image analysis. The abundance of complex, noisy, high-resolution image data is what drew me to biophysics from high energy early in my graduate career. In the past decade, machine learning applied to images has emerged as a powerful tool for analyzing the content of images with unprecedented rigor, exceeding the accuracy of human experts in many cases. The architectures that have consistently outperformed in the field of image processing are deep convolutional neural networks whose applications range from self-driving cars

and facial recognition to classifying deforestation in the Amazon Rainforest. My dissertation is focused on the intersection of biological imaging, deep learning and the gut microbiome. In particular, my work has centered around understanding two important features of intestinal microbial communities; their spatial structure, and the individual interactions between their constituents. This dissertation is composed of deep learning applications and non-imaging based experimentation. I describe work done to create and apply several deep learning algorithms to identification of bacteria and host morphologies which will, in the future, allow for study of spatial structure of these microbes within the intestine of larval zebrafish. I also describe an experiment in which we probe interspecies bacterial interactions in larval zebrafish through gut dissections and plating of contents, losing spatial information but providing precise quantitative data on the abundance of several species at once. These studies will enable future investigations that combine these advances to determine the spatial structure of these microbes interacting inside the gut, which can further decipher multispecies microbial interactions.

1.2. Imaging of Intestinal Microbiota in Larval Zebrafish

To better understand the spatial structure of the intestinal microbiota, a variety of microscopy techniques have been developed that allow for in-vivo imaging of bacteria and other microorganisms within the intestines of various animals [2, 3, 4, 5]. In this thesis, I will be discussing two of these techniques, light sheet fluorescence microscopy (LSFM) and differential interference contrast microscopy (DIC) and their use in imaging larval zebrafish and their intestinal microbes. Previous members of the Parthasarathy lab, Matthew Jemielita, Mike Taormina and Ryan Baker created a microscopy system combining both of these techniques

as discussed in [2, 6]. These systems each produce high-content, high-resolution images. It is important to have good image processing tools in order to obtain quantitative information from these images which has been the focus of much of my work in the Parthasarathy lab.

Zebrafish were introduced as a model organism by Streisinger here at the University of Oregon 40 years ago [7]. Along with *Drosophila melanogaster* (fruit fly), *C. elegans* (nematode worm), and mice, zebrafish are commonly used model organisms for the study of intestinal microbes, among many other applications [8, 9, 10, 11, 12, 13]. In contrast to *Drosophila* and *C. elegans*, zebrafish are vertebrates and thus many processes are shared with humans. Similar to *Drosophila* and *C. elegans*, zebrafish are nearly transparent in their larval stage making them amenable to live imaging in contrast to mice. While mice are more closely related to humans than zebrafish and have an abundance of genetic tools, they come at the cost of less simple husbandry as well as difficulty in non-invasively probing the intestinal microbes.

Light sheet microscopy is a technique in which an excitation laser is oscillated at a high frequency forming a time-averaged thin sheet of laser light, Fig 1.1. This sheet passes through a specimen exciting any fluorescent molecules within. These molecules then emit light of a longer wavelength than the excitation light which passes through an object which focuses the light and a band pass filter that allows through only the emitted light. After the filter, the light is picked up by a camera. One can move the sample while taking pictures creating a scan with a specific z-resolution set by the frame rate and the speed of the moving sample. One can also leave the specimen in place while taking pictures to obtain a video. In contrast to confocal microscopy which illuminates a large volume of the sample and rejects

light not in the focal point, in light sheet microscopy every part of the sample that is illuminated is imaged, Fig 1.1. This allows for diminished photobleaching and phototoxicity which in turn allows for long term imaging of specimens without significant loss of signal or damage to the specimen.

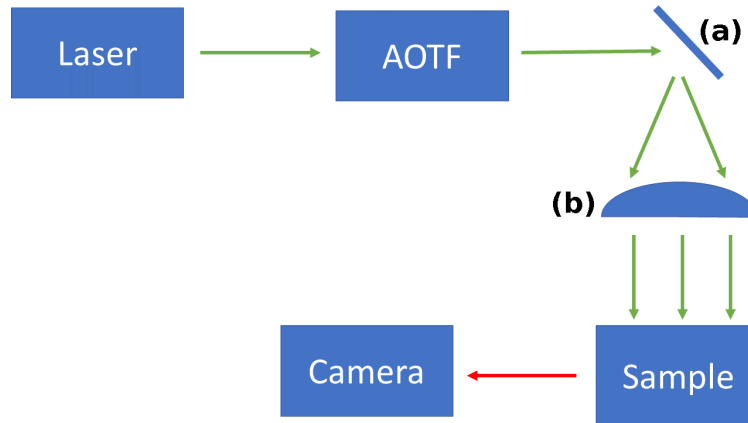


FIGURE 1.1. **Schematic of a light sheet fluorescent microscope.** A laser passes through an AOTF after which it is oscillated at a high frequency at a galvanometer (a), passes through a lens (b), then passes through a sample perpendicular to which is a camera that records the emitted light.

The Parthasarathy Lab realized that LSFMs fast, high-resolution 4D imaging allows for unprecedented study of intestinal microbes as well as their host, and for the past few years has applied this technique to study gut microbial systems in zebrafish, obtaining what are to date the only data in any animal species of in vivo gut microbial dynamics with single-bacterium resolution. Previous examples of this approach from the Parthasarathy lab include studies of the population dynamics of two strongly competing bacterial species in larval zebrafish [8, 11], the discovery that the bacterial type VI secretion system can stimulate intestinal transport and displace competing species [13], and uncovering relationships between bacterial cohesion and the spatial distribution of intestinal microbes [14].

Differential interference contrast microscopy uses transmitted light to generate optical contrast and sectioning [15, 16]. The technique as usually implemented uses a Wollaston prism to separate light of orthogonal polarizations along two different paths. The light then passes through the sample and then another prism, recombining the separated paths. Each point on the camera plane therefore combines light from two spatially separated points from the object plane and their interference depends on their relative path length. This leads to a 2-D image in which contrast is due to index of refraction gradients, emphasizing any edges. Our setup uses a single-prism technique. For a more detailed discussion as well as its integration with LSFM see [2]. In our own lab, this combined microscopy set up has allowed for quantification of gut motility in larval zebrafish [17] which enabled the discovery of intestinal microbes altering gut motility [13].

These two techniques provide high resolution images that are noisy and whose noise varies both across the image in space and time, and has complex textures (especially DIC). A single LSFM scan of one region of a zebrafish can contain hundreds of millions of pixels. A typical experiment can perform 20+ of these scans in a single day. Because of their size and complexity, it is non-trivial to obtain quantitative information from these images. Due to the natural variation in biological parameters one is interested in quantifying, a large number of samples is required making it very difficult to analyze these images with techniques that require large amounts of user input or are not computationally efficient.

1.3. Deep Learning on Images

Due to the analytic challenges noted above, one needs both automation and accurate generalization in order to quantify the information found in LSFM and

DIC images. Deep learning has emerged as a tool that can address these; I will briefly note the history of deep learning here.

In an attempt to better understand the human brain, mathematical models were created of neurons and their connections to one another. These models, or neural networks, were initially attempt to better understand the rules governing the firing of neurons within the brain but were found to be useful in other applications as well. The first practical implementation of a neural network appears to be Stanfords MADALINE, which was used to help make phone calls more clear by removing echos from the calls [18]. Despite early interest in their application, it wasnt until 2006 that excitement in these networks surged when Geoffrey Hinton published a paper [19] obtaining unprecedented accuracy on classifying hand-written numbers from the standard CIFAR dataset using what they called deep belief nets. Hinton, as well as Yoshua Bengio and Yann LeCun are largely credited for the rebirth of neural networks and the branding of the term deep learning. LeCun pioneered work on convolutional neural networks throughout the 90s and is responsible for simple gradient descent which led the way for relying on more automatic learning, and less on hand-designed heuristics [20]. LeCuns paper showed that it was possible for neural networks to be applied directly to the pixels of the images requiring no manual determination of of features thus paving the way for deep learning on images that has become a ubiquitous image classification technique.

The success of deep learning on images due to these network architecture advances as well as an explosion of image data, powerful GPUs and open-source software. Due to the rapid adoption of smartphones by people across the globe, the amount of digital pictures taken each year has increased to astonishing levels. For

instance, it is estimated that in 2018 there were around 1.2 trillion photos taken, up from 660 billion in 2013, doubling in only five years [21]. GPUs have gone from hundreds to thousands of cores with many cards specifically designed and targeted to deep learning applications, i.e. Googles Tensor Processing Units or Nvidias Tesla GPUs. There has been a large increase in open-sourced software devoted to image processing and deep learning that make creating a deep convolutional neural network or distributing its computation across a graphics card relatively easy to implement. The work of this dissertation was implemented using Tensorflow [22], Scit-Kit Learn [23], Sci-Kit Image [24] among other python packages. There are many other open-source tools that are extremely impressive like Theano [25], Keras [26], Caffe [27] and Torch [28]. Chapter II describes the application of a convolutional neural network to identify individual bacteria of several species from 3D LSM images of the intestines of larval zebrafish. This chapter contains previously published co-authored material with contributions from Raghuv eer Parthasarathy. Chapter III follows my application of the deep learning architecture U-net to segment the intestine in DIC images.

1.4. Interactions of Intestinal Microbial Communities

In 1837, Charles Cagniard-Latour, Friedrich Traugott Ktzing and Theodor Schwann [29] published three separate papers arguing that yeast in beer, or as they were referred to at the time, the sugar fungus, were living organisms and hence these three were the first to determine that the microscopic objects seen in fermenting beverages were living organisms. Twenty or so years later, Louis Pasteur developed a more comprehensive description of alcoholic fermentation when studying wine in Lille, France which led to his work on the germ theory

of disease and helped to convince the world that microbes existed and were in fact living organisms. And so it is apt that for my doctorate I have been able to further study microbes through my love for fermentation. After years of producing craft beer, I have transitioned to making wine in the Willamette Valley. It was through my interest in winemaking, in particular my intrigue into the diversity of fermentation microbes and their interactions, both directly through biochemical signals and toxins and indirectly through their impact on nutrients within the wine, that piqued my interest in studying multi-species communities within larval zebrafish.

The interactions between the members of multi-species communities inform the rules that govern the assemblage and maintenance of these communities. Despite its importance, it is not well understood how these interactions behave. At present there is a lot of theoretical interest [30, 31, 32] in multi-species systems, but relatively little experimental data, especially for the gut microbiome. The majority of studies on intestinal microbiota have been performed on naturally assembled microbiomes by sequencing DNA extracted from fecal samples. Since sequencing data provides relative, rather than absolute, microbial abundances, it is challenging to accurately infer interactions between species [30]. An alternative approach to deducing interactions from natural, complex host-microbiota systems is to build such systems from the bottom-up, using model organisms, techniques for generating initially germ-free animals, and well-defined sets of small numbers of microbial species. While there are many studies unraveling the individual biochemical interactions between microbes, it is unclear to what degree bacterial interactions can be inferred from bacterial abundance information alone for a system of multiple bacterial species. Chapter IV discusses an ongoing experiment

in which we take a bottom-up approach to quantifying the interspecies interactions of commensal bacteria within larval zebrafish. I note that the work I have done on deep learning applied to images could be tied together with these multi-species studies in future work to explore the interplay of spatial structure and bacterial interactions. The work performed in this thesis is a first step towards that end. Chapter IV contains as yet unpublished co-authored material with contributions from Raghuveer Parthasarathy, Dylan Martins, Deepika Sundarraman, Drew Shields and Noah Pettinari.

CHAPTER II

PERFORMANCE OF CONVOLUTIONAL NEURAL NETWORKS FOR IDENTIFICATION OF BACTERIA IN 3D MICROSCOPY DATASETS

This chapter contains previously published co-authored material with contributions from Raghuv eer Parthasarathy. In this work, I contributed to designing the research, performing the research, analyzing the data, and writing the paper.

2.1. Introduction

The continued development and widespread adoption of three-dimensional microscopy methods enables insightful observations into the structure and time-evolution of living systems. Techniques such as confocal microscopy [33, 34], two-photon excitation microscopy [35, 36, 37, 38], and light sheet fluorescence microscopy [3, 11, 38, 39, 40, 41, 42] have provided insights into neural activity, embryonic morphogenesis, plant root growth, gut bacterial competition, and more. Extracting quantitative information from biological image data often calls for identification of objects such as cells, organs, or organelles in an array of pixels, a task that can be especially challenging for three-dimensional datasets from live imaging due to their large size and potentially complex backgrounds. Aberrations and scattering in deep tissue can, for example, introduce noise and distortions, and live animals often contain autofluorescent biomaterials that complicate the discrimination of labeled features of interest. Moreover, traditional image processing techniques tend to require considerable manual curation, as well as user input regarding which features, such as cell size, homogeneity, or aspect

ratio, should guide and parameterize analysis algorithms. These features may be difficult to know a priori, and need not be the features that lead to the greatest classification accuracy. As data grow in both size and complexity, and as imaging methods are applied to an ever-greater variety of systems, standard approaches become increasingly unwieldy, motivating work on better computational methods.

Machine learning methods, in particular convolutional neural networks (ConvNets), are increasingly used in many fields and have achieved unprecedented accuracies in image classification tasks [20, 43, 44?]. The objective of supervised machine learning is to use a labeled dataset to train a computer to make classifications or predictions given new, unlabeled data. Traditional feature-based machine learning algorithms, such as support vector machines and random forests, make use of manually determined characteristics, which in the context of image data could be the eccentricity of objects, their size, their median pixel intensity, etc. The first stages in the implementation of these algorithms, therefore, are the identification of objects by image segmentation methods and the calculation of the desired feature values. In contrast, convolutional neural networks use the raw pixel values as inputs, eliminating the need for determination of object features by the user. Convolutional neural networks use layers consisting of multiple kernels, numerical arrays acting as filters, which are convolved across the input taking advantage of locally correlated information. These kernels are updated as the algorithm is fed labeled data, converging by numerical optimization methods on the weights that best match the training data. ConvNets can contain hundreds of kernels over tens or hundreds of layers which leads to hundreds of thousands of parameters to be learned, requiring considerable computation and, importantly, large labeled datasets to constrain the parameters. Over the past decade, the use

of ConvNets has been enabled by advances in GPU technology, the availability of large labeled datasets in many fields, and user-friendly deep learning software such as TensorFlow [22], Theano [25], Keras [26], and Torch [28]. In addition to high accuracy, ConvNets tend to have fast classification speeds compared to traditional image processing methods. There are drawbacks, however, to neural network approaches. As noted, they require large amounts of manually labeled data for training the network. Furthermore, their selection criteria, in other words the meanings of the kernels' parameters, are not easily understandable by humans [45].

There have been several notable examples of machine learning methods applied to biological optical microscopy data [46, 47], including bacterial identification from 2D images using deep learning [48], pixel-level image segmentation using deep learning [49, 50, 51], subcellular protein classification [52], detection of structures within *C. elegans* from 2D projections of 3D image stacks using support vector machines [53], and more [54, 55, 56, 57, 58]. Nonetheless, it is unclear whether ConvNet approaches are successful for thick, three-dimensional microscopy datasets, whether their potentially greater accuracy outweighs the drawbacks noted above, and what design principles should guide the implementation of ConvNets for 3D microscopy data.

To address these issues, we applied a deep convolutional neural network to analyze three-dimensional light sheet fluorescence microscopy datasets of gut bacteria in larval zebrafish (Fig 2.1 a,b) and compared its performance to that of other methods. These image sets, in addition to representing a major research focus of our lab related to the aim of understanding the structure and dynamics of gut microbial communities [8, 11, 12, 13], serve as exemplars of the large, complex data types increasingly enabled by new imaging methods. Each 3D image occupies

roughly 5 GB of storage space and consists of approximately 300 slices separated by 1 micron, each slice consisting of 6000 x 2000 pixel 2D images (975x325 microns). These images include discrete bacterial cells, strong and variable autofluorescence from the mucus-rich intestinal interior [59], autofluorescent zebrafish cells, inhomogeneous illumination due to shadowing of the light sheet by pigment cells, and noise of various sorts. The bacteria examined here exist predominantly as discrete, planktonic individuals. Other species in the zebrafish gut exhibit pronounced aggregation; identification of aggregates is outside the scope of this work, though we note that the segmentation of aggregates is much less challenging than identification of discrete bacterial cells, due to their overall brightness and size. The goal of the analysis described here is to correctly classify regions of high intensity as bacteria or as non-bacterial objects.

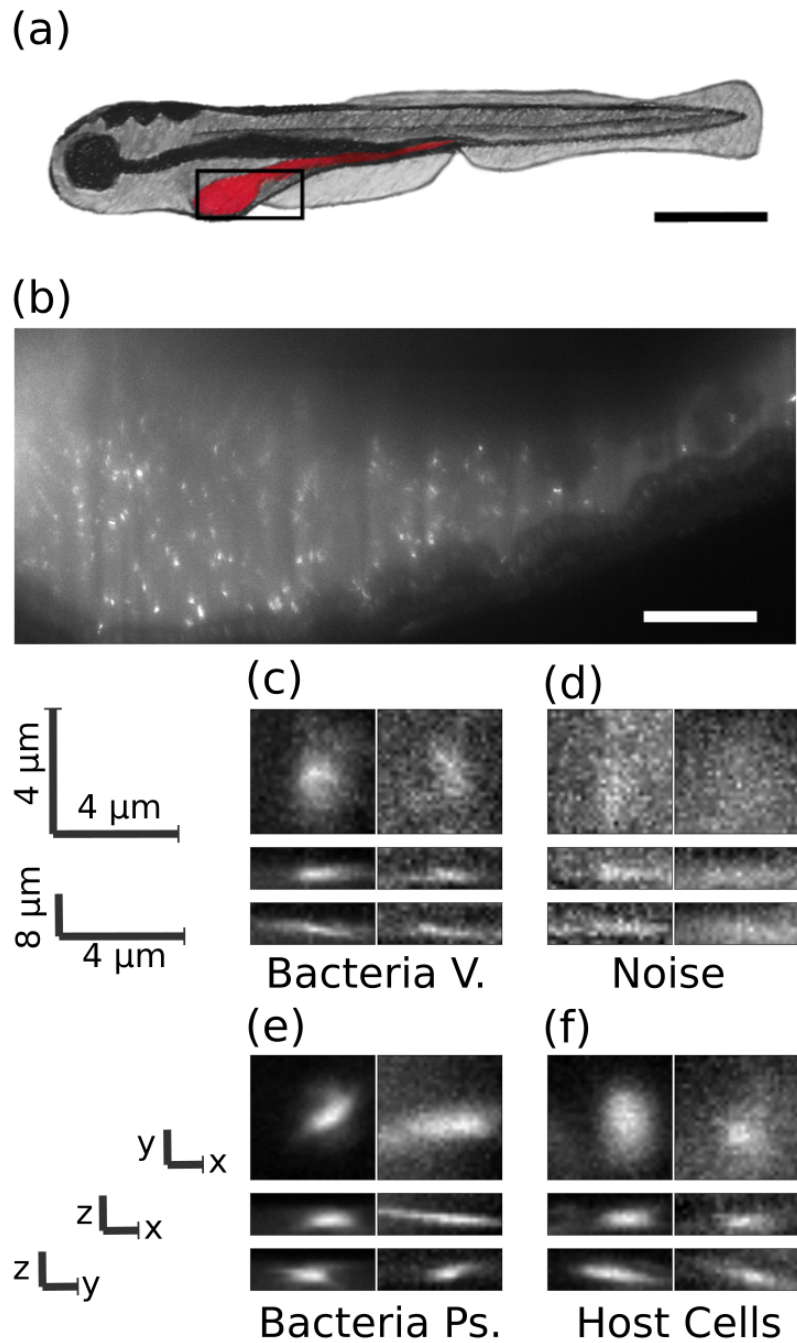


FIGURE 2.1. **Images of bacteria in the intestine of larval zebrafish.**
 a) Schematic illustration of a larval zebrafish with the intestine highlighted in red. Scale bar: 0.5 mm. b) Single optical section from light sheet fluorescence microscopy of the anterior intestine of a larval zebrafish colonized by GFP expressing bacteria of the commensal *Vibrio* species ZWU0020. Scale bar: 50 microns. c) z, y and x projections from 28x28x8 pixel regions of representative individual *Vibrio* bacteria, d) non-bacterial noise, e) individual bacteria of the genus *Pseudomonas*, species ZWU0006, and f) autofluorescent zebrafish cells.

Using multiple testing image sets, we compared the performance of the convolutional neural network to that of humans as well as random forest and support vector machine classifiers. In brief, the ConvNet’s accuracy is similar to that of humans, and it outperforms the other machine classifiers in both accuracy and speed across all tested datasets. In addition, the ConvNet performs well when applied to planktonic bacteria of a different genus through the use of transfer learning. Transfer learning has been shown to be effective in biological image data in which partial transference of network weights from 2D images dramatically lowers the amount of new labeled data that is required [44, 52, 55, 60]. We explored the impacts on the ConvNet’s performance of network structure, the degree of data augmentation using rotations and reflections of the input data, and the size of the training data set, providing insights that will facilitate the use of ConvNets in other biological imaging contexts.

Analysis code as well as all $\sim 21,000$ manually labeled 3D image regions-of-interest are provided; see Methods for details and urls to data locations.

2.2. Results

Data

The image data we sought to classify consist of three-dimensional arrays of pixels obtained from light sheet fluorescence microscopy of bacteria in the intestines of larval zebrafish [8, 11, 12, 13]. Fig 2.1B shows a typical optical section from an initially germ-free larval zebrafish, colonized by a single labeled bacterial species made up of discrete, planktonic individuals expressing green fluorescent protein; a three-dimensional scan is provided as Supplementary Movie 1. All the data assessed

here were derived from fish that were reared germ free (devoid of any microbes) [61] and then either mono-associated with a commensal bacterial species or left germ free. Nine scans are of fish mono-associated with the commensal species ZWU0020 of the genus *Vibrio* [9, 10, 11], two scans are of fish in which the zebrafish remained germ-free, and a single scan is from a fish mono-associated with *Pseudomonas* ZWU0006 [12]. For each 3D scan, we first determined the intestinal space of the zebrafish using simple thresholding and detected bright objects (blobs) using a difference of Gaussians method described further in Methods. From each blob, we extracted 28x28x8 pixel arrays (4.5x4.5x8 microns), which served as the input data to the neural network, to be classified as bacterial or non-bacterial.

Since there is no way to obtain ground truth values for bacterial identity in images, we manually classified blobs to serve as the training data for the neural network, using our expertise derived from considerable prior work on three dimensional bacterial imaging. Notably, in prior work we showed that the total bacterial abundance determined by manually corroborated feature-based bacterial identification from light sheet data corresponds well with the total bacterial abundance as measured through gut dissection and serial plating assays [8]. In Fig 2.1C-F we show representative images of blobs corresponding to bacteria and noise.

In order to estimate an upper bound on the classification accuracy we can expect from the learning algorithms, we chose a single image scan which we judged to be typical of a noisy, complex 3D image of the intestine of a larval zebrafish colonized by bacteria. We then had six lab members with least two years' experience with light sheet microscopy of bacteria individually label each of the detected potential objects as either a bacterium or not. We show in Fig 2.2A the agreement between lab members. Excluding human 3 the agreement between any

pair of humans is always above 0.87. The outlier, human 3, is the person with the least experience with the imaging data, namely the principal investigator.

We next created a set of labeled data by manual classification of blobs from the 9 *Vibrio* scans and 2 scans of germ-free fish, consisting in total of over 20,000 objects. Including scans from germ-free fish is particularly important to enable accurate counting of low numbers of bacteria, which arise naturally due to extinction events [11] and population bottlenecks [9].

Network Architecture

As detailed in Methods, we used Google’s open-source Tensorflow framework [22] to create, test, and implement 3D convolutional neural networks. Such networks have many design parameters and options, including the number, size, and type of layers, the kernel size, the downsizing of convolution output by pooling, and parameter regularization. In general, overly small networks can lack the complexity to characterize image data, though their limited parameter space is less likely to lead to overfitting. Conversely, larger networks can tackle more complex classification schemes, but demand more training data to constrain the large number of parameters, and also carry a greater computational load. In between these extremes, many design variations will typically give similar classification accuracy. We chose a simple architecture consisting of two convolutional layers followed by a fully connected layer. The first and second convolutional layers contain 16 and 32 $5 \times 5 \times 2$ kernels, respectively. Each layer is followed by $2 \times 2 \times 2$ max pooling as further described in Methods. The final layer is a fully connected layer consisting of 1024 neurons with a dropout rate of 0.5 during training. After this, softmax regression is used for binary classification.

We explored various alterations of our network architecture, and illustrate here the effect of simply varying the number of kernels per convolutional layer. We assessed the classification accuracy as a function of the number of kernels in layer 1, with the number of kernels in layer 2 being double this. Accuracy was calculated using cross validation, training on all but one image dataset (where an image dataset is a complete three-dimensional scan of the gut of one zebrafish), testing on the remaining image dataset, and repeating with different train/test combinations. The network accuracy initially increases with kernel number and plateaus at roughly 16 kernels, beyond which the variance in accuracy increases (Fig 2.2B). Therefore, increasing the number of kernels beyond approximately 16 gives little or no improvement in accuracy at the expense of model complexity and increased variability. We note that there are many ways to alter network complexity, for example adding or removing layers, all of which may be interesting to investigate. Here, a rather small model consisting of two layers is sufficient to achieve human-level accuracy, suggesting that adding layers is unlikely to be useful.

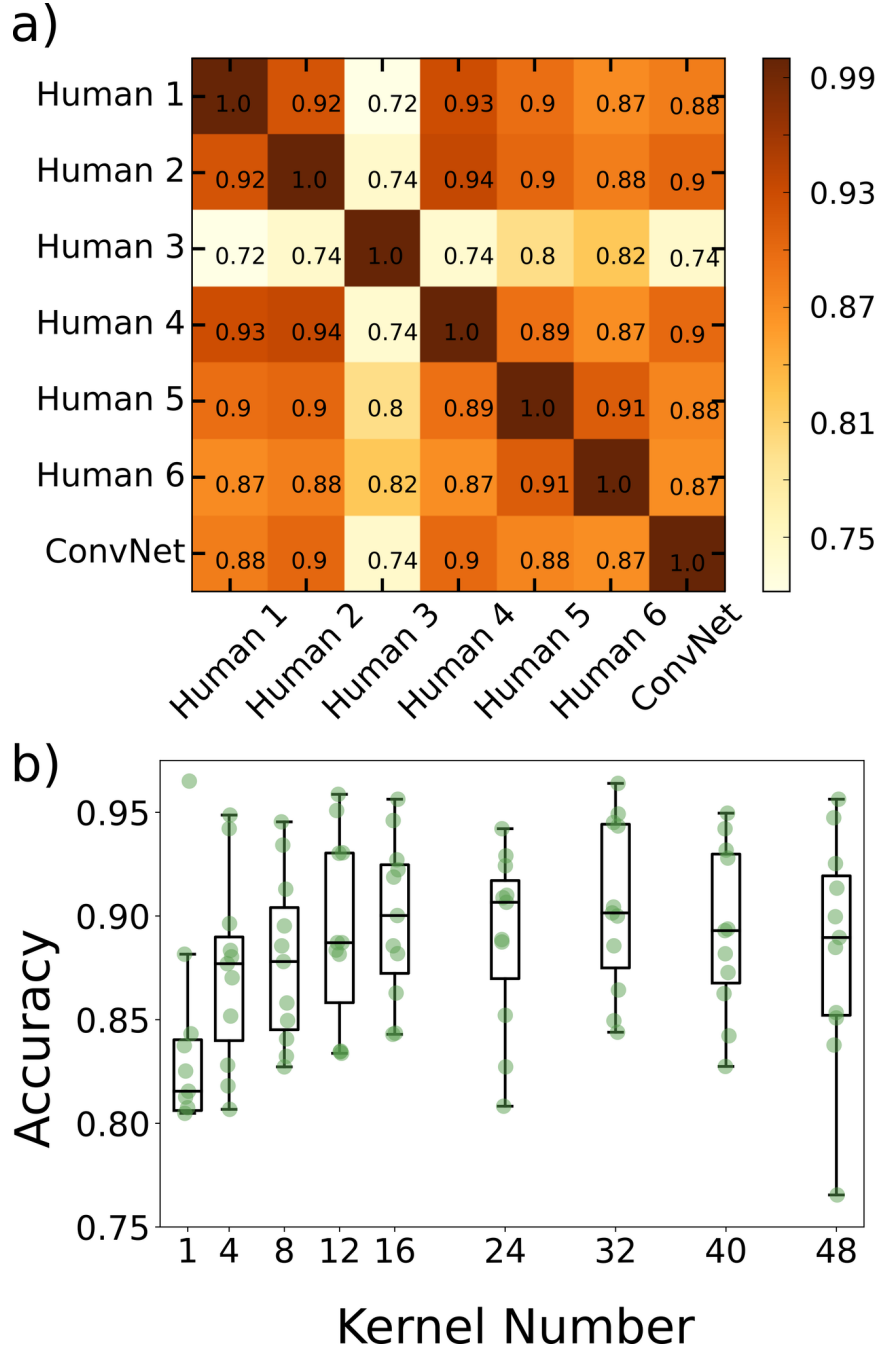


FIGURE 2.2. **Creation of the 3-D convolutional neural network.** a) Agreement matrix between six individuals (members of the authors' research group), evaluated on a single dataset of images of *Vibrio* bacteria, and between those humans and the convolutional neural network. b) Accuracy vs number of kernels per layer using cross validation across the various imaging datasets, where the x-axis denotes the number of kernels in the first convolutional layer. The second convolutional layer for each plotted point has twice as many kernels as the first.

Network Accuracy Across Image Datasets

We trained the ConvNet using manually labeled data from eight of the *Vibrio* image datasets and the two datasets from germ-free fish (devoid of gut bacteria) and then tested it on the remaining manually labeled *Vibrio* image dataset that was used to assess inter-human variability, described above. The agreement between the neural network and humans (mean std. dev. 0.89 0.01) was indistinguishable from the inter-human agreement (mean std. dev. 0.90 0.02), again excluding human 3, indicating that the ConvNet achieves the practical maximum of bacterial classification accuracy (Fig 2.2A). Examples of images for which all humans agreed on the classification, and in which there was disagreement, are provided in the Supplementary Text.

To further test the network’s consistency across different imaging conditions we applied it separately to each of the 3D image datasets of larval zebrafish intestines. We also tested, with the same procedure and data, random forest and support vector machine classifiers to address the question of whether or not the ConvNet outperforms typical feature based learning algorithms. We first consider two experiment types: zebrafish intestines mono-associated with *Vibrio* ZWU0020 (9 image datasets, i.e. 9 complete three-dimensional scans from of different zebrafish) and germ-free zebrafish (2 image datasets). Classifier accuracy for each *Vibrio*-colonized or empty-gut image scan was determined by cross-validation, training the network using all of the other image datasets, and testing on the dataset of interest. To test the variance in accuracy due to the training process, we performed three repetitions of each train/test combination using the same data.

We found that the neural network outperforms the feature based algorithms on every image dataset (Fig 2.3), and also shows less variation in accuracy between

the different datasets. The enhanced accuracy from the neural network is especially dramatic for germ-free datasets, for which it achieves over 90% accuracy, in contrast to less than 75% for feature based methods. For a given test dataset, the training variance for the convolutional neural network is small but nonzero, indicating that the network training algorithm finds similar, but not identical, minima with different (random) initializations on the same training data. It is also small for the random forest classifier. Interestingly, it is zero for the SVM classifier, indicating that given the same dataset, the algorithm is finding the same minimum.

To further verify the robustness of our accuracy measures, we performed tests using a manually labeled image dataset that was completely distinct from those previously considered, and that therefore played no role in cross-validation or other prior work. This new test set consisted of 1302 images of bacteria (482 images) or noise (840 images). We determined the classification accuracy of our convolutional neural network to be 89.3%, the support vector classifier to be 83.1 %, and the random forest classifier to be 78.5 %, in agreement with the prior assessments.

The random forest, support vector machine, and neural network classifiers process roughly 300, 400, and 950 images per second, respectively; i.e. the neural network runs 2-3 times faster than the feature based learning algorithms on the same data.

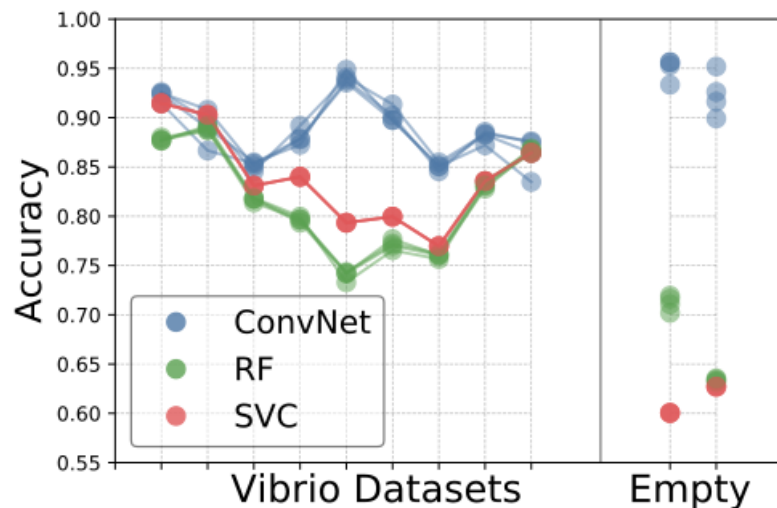


FIGURE 2.3. **Comparison of Convnet and feature based learning algorithms across all datasets.** Comparison of accuracies for the various learning algorithms (convolutional neural network, support vector classifier, and random forest) across different *Vibrio* image datasets, as well as two image datasets from fish devoid of gut bacteria. Each accuracy was determined by training on the data from all of the other datasets, and testing on the dataset of interest.

Training Size and Data Augmentation

Convolutional Neural Networks famously require large amounts of training data which must often, as is the case here, be evaluated and curated by hand. To assess the scale of manual classification required for good algorithm performance, which is a key issue for future adoption of neural networks in biological image analysis, we explored the effect on the network’s accuracy of varying the amount of training data. We set aside 25% of the images from each of the *Vibrio* and germ-free fish image scans and trained the network using an increasing number of images from the remaining data. We increased the amount of training data in two different ways. First, we consecutively added to the training set all images from each image dataset excluding a subset of the images previously reserved for testing (labeled

“New datasets” in Fig 2.4A). Second, we randomly shuffled the training images from all the image scans, adding 1500 images to the training set over each iteration (labeled “Train/test split” in Fig 2.4A). For the first method, enlargement of the training set corresponds to a greater amount of data as well as data from more diverse biological sources. For the second, data size increases but the biological variation sampled is held constant. In both cases, accuracy plateaus at a number of images on the order of 10,000 (Fig 2.4A). The rise in accuracy with increasing training data size is only slightly more shallow with the first method, surprisingly, demonstrating that within-sample variation is sufficient to train the network.

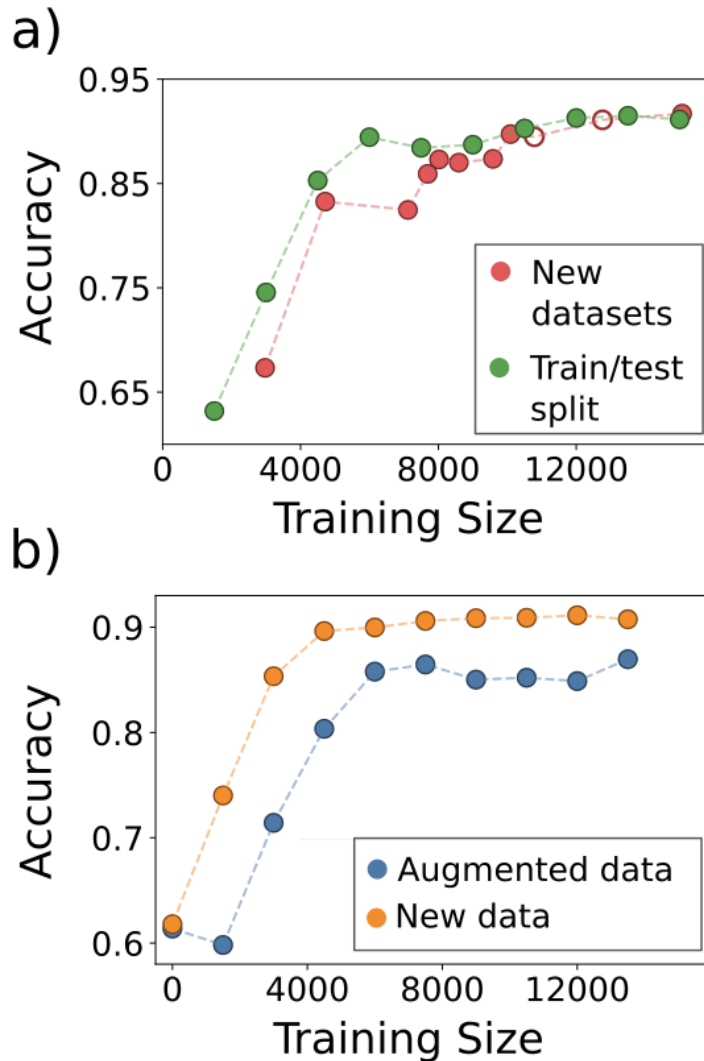


FIGURE 2.4. **Data augmentation.** Examining the accuracy of the CNN as a function of a) varying the training data size by adding images from biologically distinct datasets (New datasets) or by adding images randomly from the full set of images (Train/test split), and b) transformation of the data by image rotations and reflections

. In (a), the two empty circles represent the inclusion of the datasets from empty (germ-free) zebrafish intestines.

Data augmentation, the alteration of input images through mirror reflections, rotations, cropping, and the addition of noise, etc., is commonly used in machine

learning to enhance training dataset size and enable robust training of neural networks. To characterize the utility of data augmentation for 3D bacterial images, we focused in particular on image rotations and reflections, because the bacteria have no preferred orientation and hence augmentation by these methods creates realistic training images. We note that data augmentation is not necessary for feature based learning methods in which parity and rotational invariance can be built into the features used for classification. Obviously, augmented data is not independent of the actual training data, and so does not supply wholly new information. We were curious as to how including rotated and reflected versions of previously seen data compares, in terms of network performance, to adding entirely new data, a comparison that is useful if evaluating the necessity of performing additional imaging experiments. To test this, we compared the accuracies of the network when adding new data to that when adding rotated and reflected versions of existing data. We started with a fixed number of 1500 total objects randomly sampled from the entire set and, in the case of including new data, added another random 1500 objects at each iteration. For the augmented data, we applied random rotations and reflections to the original 1500 objects to iteratively increase the training size by 1500 objects. Each trained network was tested on the same test set of objects as that of Fig 2.4A. As shown in Fig 2.4B, the addition of new data leads to a plateau in accuracy of roughly 90% while for augmented data the plateau value is around 88%. This result demonstrates that, in the context of our network, simply augmenting existing data can raise classification accuracy to nearly the optimal level achieved by new, independent data.

Transfer Learning

We assessed the accuracy of the convolutional neural network on images of discrete gut bacteria of another species, of the genus *Pseudomonas*. Training solely on the *Vibrio* images and testing on *Pseudomonas* gives $\sim 75\%$ accuracy (Fig 2.5). However, this is much lower than the $\sim 85 - 95\%$ accuracy obtained on *Vibrio* images (Fig 2.4); the *Pseudomonas* species is not an exact morphological mimic of the *Vibrio* species. The *Pseudomonas* dataset is small (1190 images); using 80% of its images for de novo neural network training gives $\sim 72\%$ accuracy in identifying *Pseudomonas* in test datasets (Fig 2.5). We suspected that the general similarity of each species as rod-like, few-micron-long cells would allow transfer learning, in which a model trained for one task is used as the starting point for training for another task [62, 63]. Using the network weights from training on *Vibrio* image datasets, as before, as the starting values for training on the small *Pseudomonas* dataset gives over 85% accuracy in classifying *Pseudomonas* (Fig 2.5).

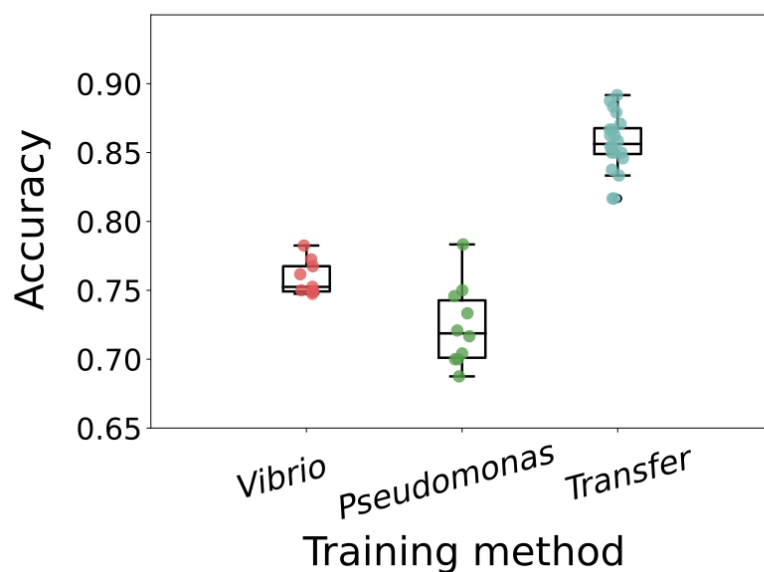


FIGURE 2.5. **Transfer learning on new bacterial sSpecies.** The accuracy of Pseudomonas classification with convolutional neural networks trained in different ways. “Vibrio” indicates training on images of Vibrio bacteria, “Pseudomonas” indicates training on the small Pseudomonas image dataset, and “Transfer” indicates using the Vibrio-derived network weights as the starting point for training on Pseudomonas images. For training only on Vibrio images, the different data points come from random weight initialization, random data ordering, and random augmentation. For training only on Pseudomonas images, and for transfer learning, the different data points are from random train/test splits of the Pseudomonas data.

2.3. Discussion

We find that a 3D convolutional neural network for binary classification of bacteria and non-bacterial objects in 3D microscopy data of the larval zebrafish gut yields high accuracy without unreasonably large demands on the amount of manually curated training data. Specifically, the convolutional neural network obtains human-expert-level accuracy, runs 2-3 times faster than other standard machine learning methods, and is consistent across different datasets and across planktonic bacteria from two different genera through the use of transfer learning.

It reaches these performance metrics after training on fewer than 10,000 human-classified images, which require approximately 20 person-hours of manual curation to generate. Moreover, augmented data in the form of rotations and reflections of real data contributes effectively to network training, further reducing the required manual labor. Experiments of the sort presented here typically involve many weeks of laboratory work. Neural network training, therefore, is a relatively small fraction of the total required time.

In many biological imaging experiments, including our own, variety and similarity are both present. Multiple distinct species or cell types may exist, each different, but with some morphological similarities. It is therefore useful to ask whether such similarities can be exploited to constrain the demands of neural network training. The concept of transfer learning addresses this issue, and we find that applying it to our bacterial images achieves high accuracy despite small labeled datasets, an observation that we suspect will apply to many image-based studies. Transfer learning is a rapidly growing area of interest, with an increasing number of tools and methods available. There are likely many possibilities for further performance enhancements to network performance via transfer learning, beyond the scope of this study. One commonly used approach is to train initially on a large, publicly available, annotated dataset such as ImageNet. It is not likely that ImageNet's set of two-dimensional images of commonplace objects will be better than actual 3D bacterial data for classifying 3D bacterial images. Nonetheless, it would be interesting to examine whether training using ImageNet or other standard datasets could establish primitive filters on which 3D convolutional neural networks could build. In addition, given the rapid growth of machine learning approaches in biology, it is likely that large, annotated datasets of

particular relevance to tasks such as those described here will be developed, further enabling transfer learning.

Though the data presented here came from a particular experimental system, consisting of fluorescently labeled bacterial species within a larval zebrafish intestine imaged with light sheet fluorescence microscopy, they exemplify general features of many contemporary three-dimensional live imaging applications, including large data size, high and variable backgrounds, optical aberrations, and morphological heterogeneity. As such, we suggest that the lessons and analysis tools provided here should be widely applicable to microbial communities [64] as well as eukaryotic multicellular organisms.

We expect the use of convolutional neural networks in biological image analysis to become increasingly widespread due to the combination of efficacy, as illustrated here, and the existence of user-friendly tools, such as TensorFlow, that make their implementation straightforward. We can imagine several extensions of the work we have described. Considering gut bacteria in particular, extending neural network methods to handle bacterial aggregates is called for by observations of a continuum of planktonic and aggregated morphologies [12]. Considering 3D images more generally, we note that the approach illustrated has as its first step detection of candidate objects (blobs), which requires choices of thresholding and filtering parameters. Alternatively, pixel-by-pixel segmentation is in principle possible using recently developed network architectures [65, 66], which could enable completely automated processing of 3D fluorescence images. In addition, pixel-based identification of overall morphology (for example, the location of the zebrafish gut) could further enhance classification accuracy, by incorporating

anatomical information that constrains the possible locations of particular cell types.

2.4. Future Directions

Since the publication of the above work, we have labeled more image data, including many images of each of the species considered in Chapter 4. Through transfer learning, this has allowed for accurate identification of each of these five bacterial species. We are currently working to implement this single bacteria identifier in combination with machine learning based algorithms to identify and segment all of the bacterial clusters within an image as well as a full segmentation of the 3D volume of the intestine, eliminating a great deal of image processing that is presently done manually. This automation will allow for unprecedented study of the spatial distributions of these bacterial species and will be a natural extension of the work described in Chapter III of this thesis.

CHAPTER III

SEMANTIC SEGMENTATION

3.1. Introduction

In trying to identify objects within complex, noisy biological image data, one is often interested in identifying exactly which pixels within an image belong to which object, a process known as semantic segmentation. Differentiating tumors from healthy organ tissue within CT scans, abnormal brain lesions from healthy brain tissue, or outlining an immune cell in a histological slide fall under this category. Prior to the recent explosion of deep learning, there were many techniques like simple thresholding, various clustering methods, and edge detection that were employed with varying degrees of success but, at least for noisy complex images, all required extensive manual curation and did not generalize well.

The initial attempts to realize semantic segmentation using deep learning were performed using convolutional networks where the input image was the neighboring pixels of a specified area centered around the pixel whose class one wanted to determine [65]. In this manner, one would apply the network pixel by pixel in a sliding window, classifying only a single pixel at a time to be of a particular object as in figure 3.1. This algorithm was originally applied to segment neuronal membranes from electron microscopy images with a great improvement over previous competitors submissions to the ISBI 2012 EM Segmentation Challenge [67]. It was quite generalizable as it required only hand labeled data and no user determination of features. Despite its success compared with conventional

segmentation methods, the technique is computationally expensive requiring as it does rastering over the entire image labeling pixel-by-pixel with redundancy in the overlap. It also suffers in accuracy as it only uses information from neighboring pixels, ignoring the rest of the images content entirely when making a classification.

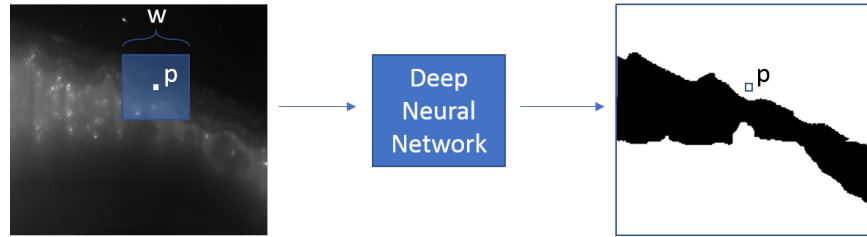


FIGURE 3.1. **Pixel-by-pixel segmentation using convolutional neural network.** Left is the input image with a window of width and height w at the center of which is the pixel to be classified. This window is passed through a convolutional neural network, center, which classifies the pixel as belonging to an object, in this example, gut or not-gut.

To decrease computational cost as well as include information from a larger region than just the neighboring pixels, another architecture called a “fully convolutional network” [68] was developed, Fig 3.2. This network consists of a series of contracting convolutional layers followed by an equal number of upsampling or transposed convolutional layers. In contrast to the previously described network, this network takes in the entire image to be segmented and outputs a segmentation of the full image in one pass. The lowest convolutional layer, just prior to upsampling, is dimensionally reduced from the input image due to the max pooling layers, in which one downsamples by taking the maximum value in an $n \times n$ patch. Therefore, much of the information that is lost in the downsampling convolutional side of the network is not retrieved in the upsampling layers. This architecture does have the benefit though of segmenting an entire image in a single pass as contrasted with the pixel-wise approach.

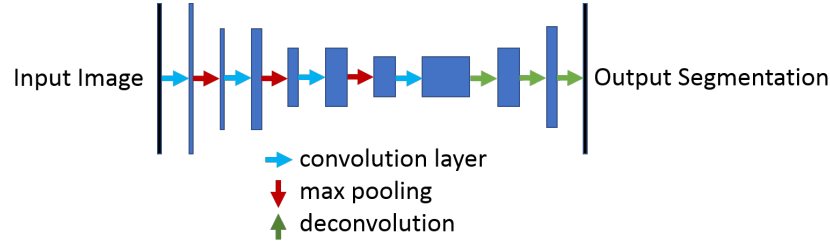


FIGURE 3.2. **Example “fully convolutional network” used for segmentation.** The image passes through a series of convolutional layers each followed by max pooling. After this, upsampling in the form of backwards convolution (deconvolution) is performed in series yielding a segmentation map.

In 2015, Ronneberger, Fischer and Brox of the University of Freiburg proposed an elegant solution [66] to the loss of information in the downsampling layers, which has since become one of the mostly widely used networks in semantic segmentation. They devised a new architecture for semantic segmentation, called U-net, that overcame the issue of high computational expense, the loss of full image context, and the large amounts of hand labeled image data required. They extended the concept of the fully convolutional network by concatenating the output of each of the contracting convolutional layers with the corresponding upsampled layers of equal sizing, Fig 3.3. Thus, their network did not suffer from the dimensionally reduced loss of information of the original fully convolutional network approach. A further discussion of the architecture follows in the next section.

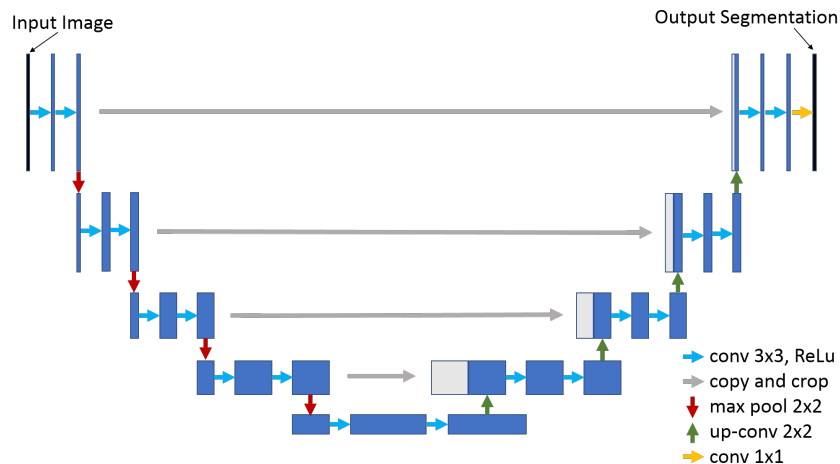


FIGURE 3.3. **Schematic of the U-net architecture.** Similarly to the “fully convolutional network”, a series of convolutional layers and max pooling are performed followed by a series of up-convolutions. U-net also concatenates the contracting path to the expanding path.

In the Parthasarathy lab, we work with 3D fluorescence microscopy images of larval zebrafish with both fluorescently labeled host cells and inoculated fluorescent bacteria [2, 6, 11, 12, 13, 14]. We also generate differential interference contrast microscopy videos of the intestines of larval zebrafish which allows for the study of gut motility. These two methodologies produce high content images with many objects one may want to segment. The images are noisy, with variable signal to noise ratio across the image in both space and time. I describe in this dissertation segmentation of these types of images, though the method is straightforward to extend to other segmentation problems, which will be discussed at the end of this chapter. I have also implemented my own version of U-net using Python and Tensorflow which allows for easy alteration of the network architecture.

3.2. U-net’s Architecture and Our Implementation

U-net, as originally implemented in Ronneburger, Fischer and Brox paper [66], is schematically illustrated in Fig 3.3. The design is similar to that of an autoencoder, another type of neural network. U-net begins with a series of convolutional layers each of which is followed by max pooling, after which a series of up-sampling and convolutional layers are employed. Note that this is nearly identical to the network described previously but in contrast, each convolutional layer from the down-sampling layer of same dimensionality is concatenated to the up-sampled layer prior to convolutions. This appending allows for the weights of the neurons in the downsampling layers to be appended to the upsampling layers, bypassing the max pooling operations. This clever implementation allows for signal to propagate across at each dimensionally reduced layer thus avoiding the loss of information a network without these connections would have. The algorithm uses valid padding in the max pooling layers so that, by the output layer in U-net, there is a loss of border pixels. To overcome this edge loss and make sure that the entire input image is segmented U-net needs to be provided with an image that has been mirror padded to the appropriate size so that the segmented image is of same dimensions as the input image before padding. The original implementation of U-net uses was constrained in several ways so as to be implemented on a standard Nvidia GPU. The input image was divided into smaller images, or tiles, using padding where needed to ensure that each tile was of equal size. The second computational limitation was the use of a batch size of one. To avoid jumps in gradient descent caused by the loss being computed from individual images at a time without the averaging one gets with a large batch size, a high momentum (0.99) is used so that many of the previous training samples are included in the

optimization step. The loss was determined using pixel-wise cross entropy and a weight map was included in which particular sets of pixels on the image could be given varying degrees of importance if say one wanted to make sure that the algorithm was properly differentiating the same cell types that were adjacent in an image. Lastly, in order to make the most of training samples, they implemented data augmentation in the form of translations, rotations, grey value variations and random elastic deformations.

My goal was to create a readily usable version of U-net and test it on gut image data. The original U-net algorithm was implemented in Caffe [27]. Tensorflow was released several months before U-net's publication and has since become the dominant deep learning software with a strong community, widespread use, heaps of documentation and easy integration with Python. Because of these reasons I decided to implement a version of U-net written in Python and using Tensorflow to build the network. My implementation of U-net closely follows that of the original paper. The code allows for variable total network depth as a depth of three works for many simple segmentation problems and has lower computational requirement than the depth of four from the original paper. For the same reason the number of kernels in the first layer is variable while the others follow the same schema of doubling after each pooling layer and halving after each up-sampling layer. The code uses cross entropy for its loss function but this can be replaced with dice loss especially in cases in which there is a significant imbalance in class weights. There is a tiling functionality that can be used as in the original paper though this may be unnecessary, especially in cases in which the segmentation problem is simple enough and downsampling of the image can reduce the image and network size to a reasonable limit.

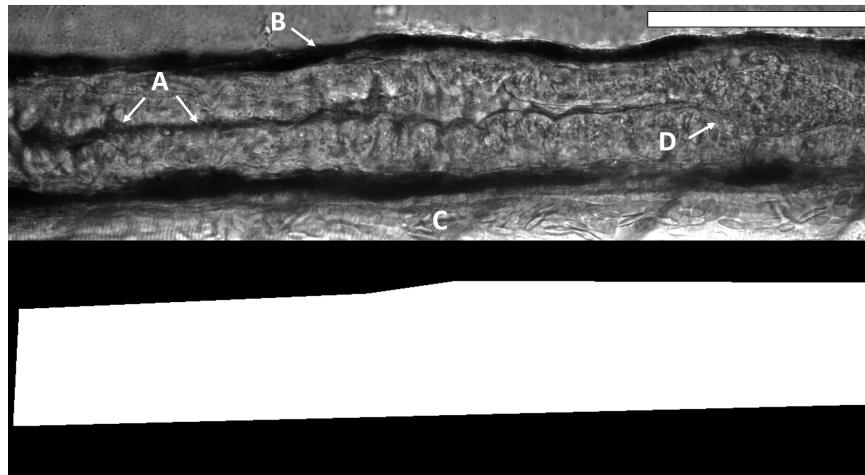


FIGURE 3.4. **DIC gut image with corresponding polygon mask.** Example DIC image with polygon from Ryan Baker’s software. (A) labels a closed lumen, (B) labels interstitial fluid, (C) muscle tissue and (D) is a luminal opening containing a bacterial bolus. The scale bar is $100 \mu m$.

3.3. Results

The intestine uses periodic contractions along its length for the transport of materials. Using DIC one can image these periodic contractions in larval zebrafish generating video from which one can abstract quantitative information characterizing this gut motility. To this end, Ryan Baker, a former graduate student in the Parthasarathy lab, created software [17] for analyzing gut motility. In this software, the intestine is first outlined by hand creating polygons that have only several points along the width of the image which is roughly 2,500 pixels in length at a scale of 0.1625 microns per pixel, see Fig 3.4. The pixels interior to these polygons are used to calculate a velocity field over time. The magnitude of the dominant modes in Fourier space are determined from which one can obtain both frequency and amplitude information thus enabling quantification of gut motility. Currently, the software requires the user to approximate the intestinal

outline using a polygon drawn on to the first frame of the video which are typically several hundred to thousands of frames in length. There are several issues with this technique; it requires manual curation by the user, the fish can drift during the course of imaging rendering the original polygon incorrect, and it does not distinguish between the intestinal lining and the lumen, or interior of the gut. This last point is particularly important in fish in which the luminal opening is large either due to a bacterial aggregate, food, or a host genetic mutation. Fig 3.5 Shows 10 example images taken from videos from different larval zebrafish. Note the variable lumen sizes, thickness of intestinal lining, blurriness, pixel intensities and gut contents.

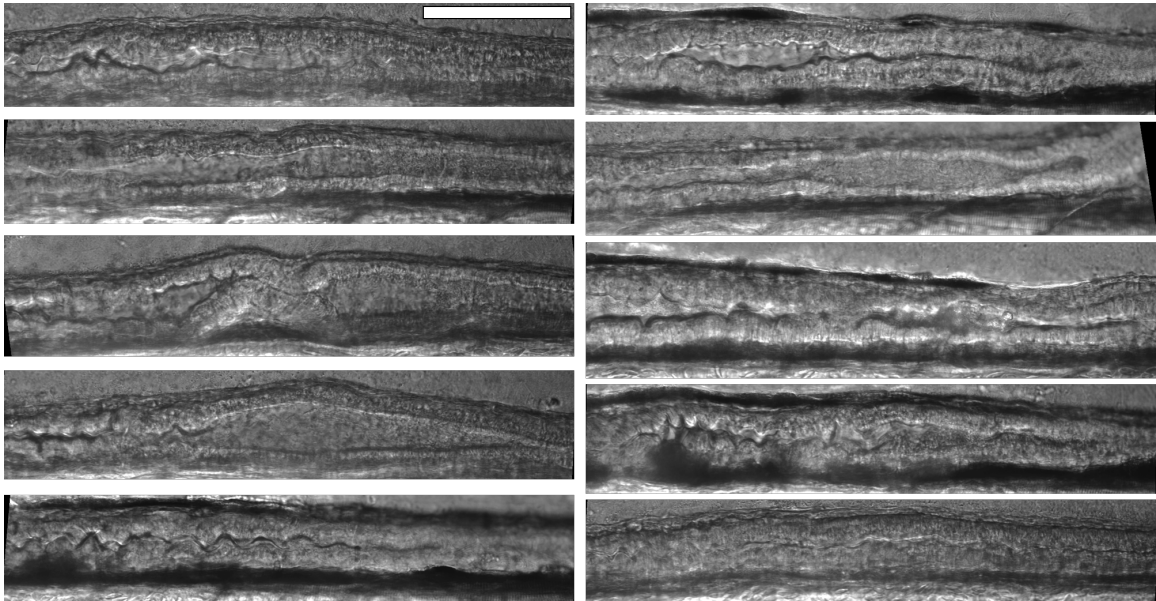


FIGURE 3.5. Example DIC gut images showing variable noise and quality. Each image is of a different fish. The scale bar is $100 \mu m$.

To address the previously mentioned issues, I was interested in applying U-net to enable segmentation that requires no user input, could more precisely outline the intestine and track any drift in the intestine over time. I trained U-net with a network depth of 3 and 32 kernels in the initial layer, using 480 hand labeled

images taken from 48 different videos of larval zebrafish intestines. In addition to visually examining the output, I also quantified the algorithm’s segmentation using images from 2 separate fish not contained in the training data, comparing with manual (human) segmentation performed by two people. The resulting segmentation is shown in Fig 3.6. The accuracy was evaluated by calculating the dice loss,

$$dice = 1 - \frac{2 \times |X \cap Y|}{|X| + |Y|}, \quad (3.1)$$

where X and Y represent the set of pixels identified as gut or exterior pixels respectively. U-net’s segmentation does quite well, especially considering the large variance in intensity in the image on the left of Fig 3.6 as well as the significant blurring and large luminal space on the image on the right. The dice loss in between U-net and the two humans for the closed lumen example on the left of Fig 3.6 is 0.48 for both while the dice loss between humans is 0.46. For the more challenging, open-lumen image on the right, the dice loss is higher between U-net and each human (0.104, 0.092) than between the two humans (0.081).

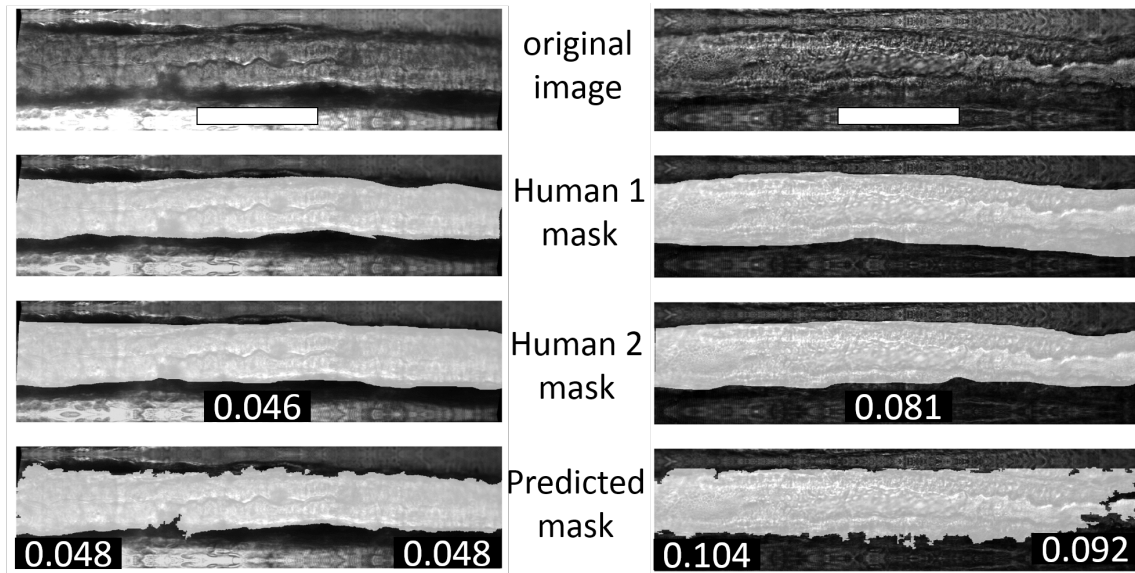


FIGURE 3.6. **U-net segmentation on DIC gut images.** DIC image followed by two different human's masks and finally the predicted mask using U-net. The dice loss is given between the two human's on the Human 1 mask panel. The dice losses between U-net and human 1 and human 2 are shown on the left and right respectively of each U-net image. The scale bars are $100 \mu m$.

In an attempt to avoid the issue of tracking the luminal space, we created masks of each of the 480 images in which the lumen was excluded from the mask of the gut as displayed in Fig 3.7. Using a deeper version of U-net (depth=4), and starting with 32 kernels in the first layer, U-net is able to differentiate lumen from gut with a lower dice loss between it and each human (0.174, 0.215) than the dice loss between the two humans (0.235) in the image with the open lumen implying that the automated segmentation is at least as good as human identification of the gut.

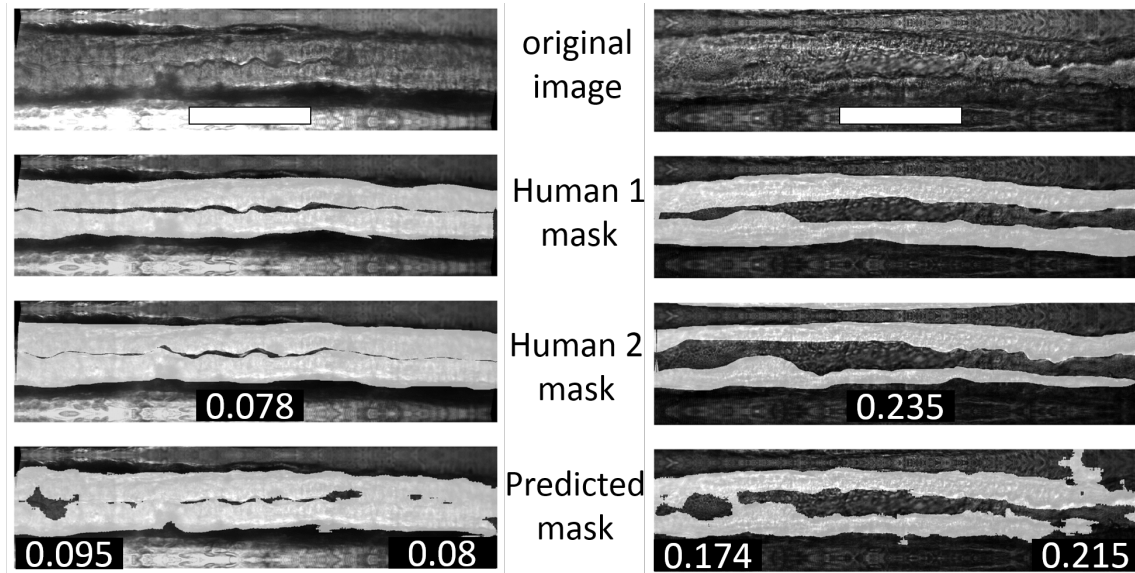


FIGURE 3.7. **U-net segmentation on DIC gut images excluding lumen.** DIC image followed by two different human’s masks and finally the predicted mask using U-net of the intestine excluding the lumen. The scale bars are $100 \mu m$.

3.4. Discussion

The resulting segmentation using U-net is certainly more accurate and automated than the current practice of creating a single polygon for each movie. It also has the potential to be immune to drift as was lacking in the previous technique. Having the segmentation hug the intestinal lining may allow for a new metric for quantifying gut motility that relies directly on the intestinal shape instead of using particle image velocimetry of the entire image. Insensitivity to the contents of the lumen will allow for a more accurate quantification of gut motility, not confounded by the dynamics of gut contents, enabling studies of gut motility in fed fish, or fish with unusual microbial communities, both of which are presently very challenging. Furthermore, tracking the lumen and its contents could allow for better quantification of the mechanics of intestinal transport which are crucial to the biophysics of intestinal populations.

CHAPTER IV

MULTI-SPECIES MICROBIAL INTERACTIONS IN LARVAL ZEBRAFISH

This chapter contains as yet unpublished co-authored material with contributions from Raghuveer Parthasarathy, Dylan Martins, Deepika Sundarraman, Drew Shields and Noah Pettinari. In this work, I contributed to designing the research, performing the research, analyzing the data, and writing the paper.

4.1. Introduction

Intestinal microbes exist in diverse, highly complex and heterogeneous communities containing dozens to hundreds of taxonomically diverse species including viruses, eukaryotes, archaea and prokaryotes. The composition of these communities varies across individuals and is crucial to the health of the host, having been shown to be correlated with a wide range of diseases [69, 70], the development of various organs [71, 72], and immune regulation [73]. Despite the importance of these intestinal communities, the determinants of their composition remain largely unknown. The vast majority of studies on intestinal microbiota have been performed on naturally assembled microbiomes by sequencing DNA extracted from fecal samples. Though this approach provides powerful insights into the species and genes present in the gut, it suffers from severe limitations. For example, one is sampling only the microbes that have exited the host, which may not be representative of the intestinal community [74]. Furthermore, sequencing data typically provide relative, rather than absolute, microbial abundances, from which it is fundamentally challenging to accurately infer interactions between species [30].

Our lack of understanding of the rules governing the composition of these intestinal microbial communities hinders our ability to deliberately alter these communities for therapeutic ends.

An alternative approach to attempting to deduce interactions from natural, complex host-microbiota systems is to build such systems from the bottom-up, using model organisms, techniques for generating initially germ-free animals, and well-defined sets of small numbers of microbial species. Recent work along these lines has been performed using the nematode *C. elegans* [75] and the fruit fly *D. melanogaster* [76, 77], described further below. However, it is unclear whether these results translate to a vertebrate gut, which has both greater anatomical complexity and more specific microbial selection [9]. To address this, we implement a bottom-up approach of measuring bacterial interactions in larval zebrafish, Fig 4.1 (a), a model organism amenable to gnotobiotic techniques [61, 78], which has enabled in earlier work delineation of specific interbacterial competition mechanisms related to intestinal transport [11, 13] as was discussed in the Introduction.

A key question for understanding microbial community assembly is whether inter-species interactions, either cooperative or competitive, are pairwise additive. In other words, is characterization of interactions between all pairs of microbial species sufficient to explain outcomes when more than two species are present, or are higher-order interactions important? Recent work using well-defined bacterial assemblies in *Drosophila melanogaster* found significant higher-order interactions, influencing host traits such as lifespan [76]. In contrast, analogous experiments in *C. elegans* showed that interactions could be considered pairwise additive, with a high level of predictivity for several-species communities given two-species data [77].

To assess inter-microbial interactions in the zebrafish gut, especially with respect to evaluating the potential role of higher-order interactions, we performed inoculations of initially germ-free larval zebrafish with specific subsets of five different species of bacteria and assessed the absolute abundance of each species two days post-inoculation. The five species are phylogenetically distinct, Fig 4.1 (c), and are native to and commonly found in the zebrafish gut [10]. Though the number of species is considerably fewer than the hundreds that may be present in a normal zebrafish intestine, it is large enough to sample a range of higher-order interactions, yet small enough that the possible permutations of species is tractable. As detailed below, we find strong pairwise interactions between certain bacteria. However, we find weaker interactions and a much higher than expected level of multi-species coexistence in fish colonized by 4 or 5 bacterial species. This suggests that measurements of pairwise inter-microbial interactions are insufficient to predict the composition of multispecies gut communities, and that higher-order interactions may dampen strong competition.

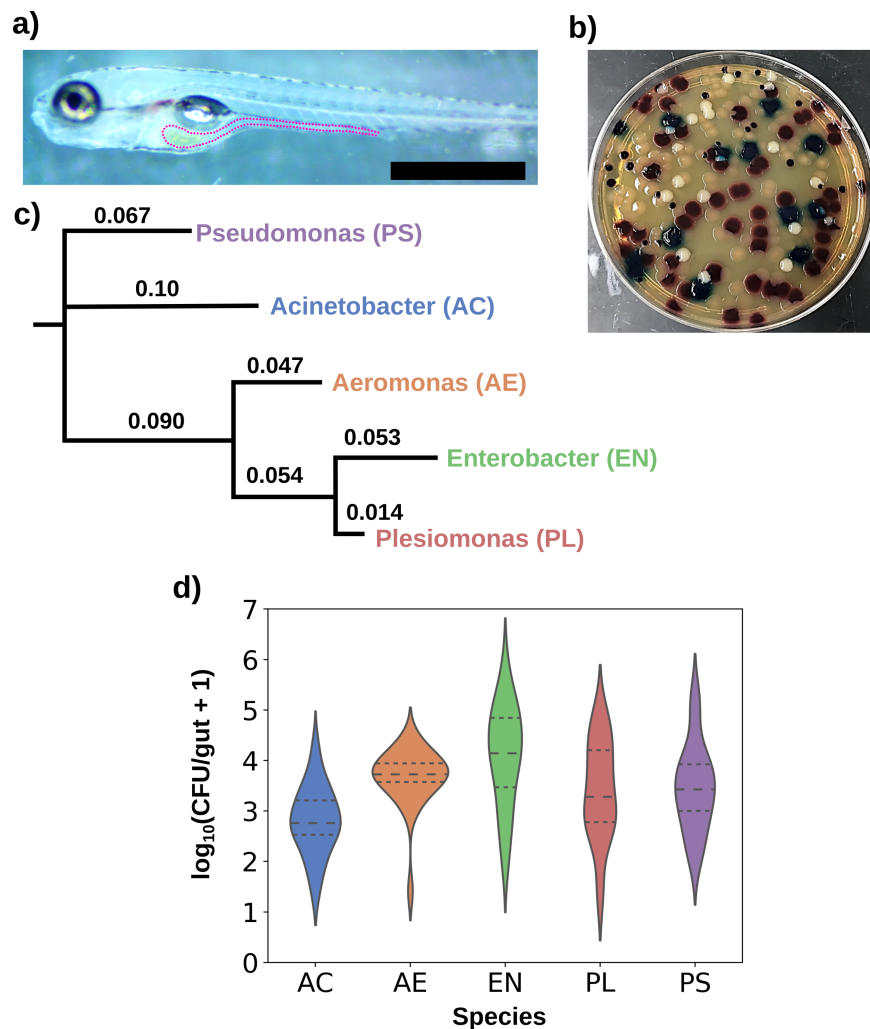


FIGURE 4.1. Image of larval zebrafish and bacterial species investigated. (a) A 7 day post fertilization larval zebrafish; the dotted curve outlines the intestine. Scale bar: 500 μm . (b) photograph of all five bacterial species plated on HiChrome universal agar on which all five species can be seen to grow to different colors and morphologies (c) Phylogenetic tree of the five bacterial species used in the experiment, also indicating the color scheme and abbreviations used throughout the text. Numbers indicate [whatever] metric of genetic distance. (d) The abundance per zebrafish gut of each of the five bacterial species when colonized in mono-association with the host, assessed as colony forming units (CFU) from plated gut contents. The violin plots indicate the distribution of CFU values, with the median and quartiles indicated by dashed lines, in $N = [35, 26, 18, 25, 25]$ fish (left to right).

4.2. Methods

Zebrafish were derived to be germ-free and housed in 15 mL flasks containing 5-15 fish. At 5 days post-fertilization (dpf) the fish were inoculated with the desired combination of microbial species by addition of bacteria to the flasks housing the fish to a density of roughly 10^6 cells/mL. The five bacteria used in this experiment were isolated from zebrafish at the University of Oregon's Zebrafish Facility. They are *Enterobacter* sp. ZOR0014, *Pseudomonas mendocina* ZWU0006, *Aeromonas* sp. ZOR0001, *Acinetobacter calcoaceticus* ZOR0008, and *Plesiomonas* sp. ZOR0011. Approximately 48 hours after inoculation, fish intestines were removed by dissection, a process done by hand under a microscope. Following dissection, the gut was placed in 500 μ L of sterile embryo medium (EM) and the contents were homogenized by vortexing the gut with the addition of zirconium oxide pellets. The slurry was then diluted by each a factor of ten and a factor of one hundred and then 100 μ L from each of these dilutions were plated onto HiCrome Universal agar from Sigma Aldrich. In this media, secreted enzymes from each of the five candidate bacterial species generate particular colors due to substrates in the chromogenic medium, allowing quantification of colony forming units (CFUs), Fig 4.1 (b). With the dilution factors used, this yields a detection limit of roughly of 25 bacteria per gut, and therefore we can obtain the absolute intestinal abundance of each of the five bacterial species in any combination.

4.3. Results

This experiment is ongoing and so as a result, interpretations presented in this dissertation are subject to change. In particular, additional data on mono-association abundances for the five species studied here may clarify their mean

values and distributions, affecting the inference of interaction parameters as described below. Nonetheless, the conclusions as presented are drawn from a large body of data, and we think large changes of interpretation are unlikely.

As noted earlier, the five species examined in this experiment were selected as diverse representatives of genera commonly found in the zebrafish intestine. We will refer to these through most of the text by genus name or two letter abbreviation: Acinetobacter (AC), Aeromonas (AE), Enterobacter (EN), Plesiomonas (PL), and Pseudomonas (PS). As expected, each species in mono-association, i.e. as the sole species inoculated with germ-free fish, colonizes robustly to an abundance of $10^3 - 10^4$ CFU/gut, corresponding to an in vivo density of approximately $10^9 - 10^{10}$ bacteria/ml Fig 4.1 (d).

We first examined all ten possible co-inoculations of five species, which enables assessment of interactions between pairs in the absence of higher-order effects. Assessment of intestinal CFUs shows a wide range of outcomes for different species pairs, indicating a range of interaction strengths. As exemplars, the CFUs per gut for two of these species, AE and EN in the presence of each of the other four, are displayed in Fig 4.2 (a) and (b) respectively. The abundance of Aeromonas is similar in the presence of any other species as it is in mono-association. In contrast, the mean Enterobacter count is similar to its mono-association value if co-inoculated with Plesiomonas or Pseudomonas, but orders of magnitude lower if co-inoculated with Acinetobacter or Aeromonas, implying in the latter causes strong negative interactions.

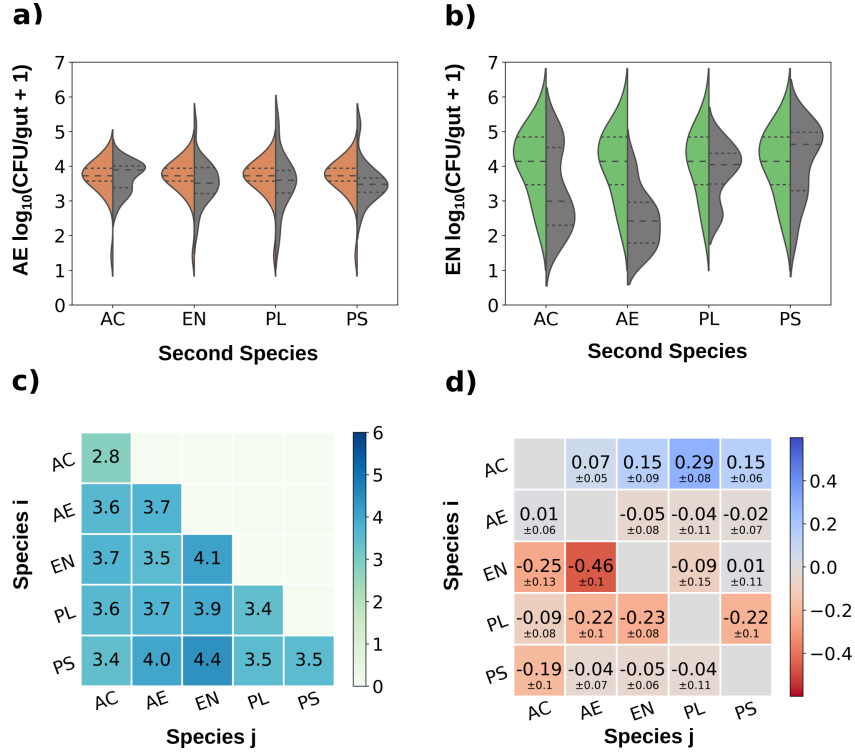


FIGURE 4.2. **Pairwise bacterial interactions.** Split violin plots of the abundances per zebrafish gut of (a) AE and (b) EN in mono-association (left curve, repeated in each plot) and in di-association with each of the other bacterial species (right curve). Medians and quartiles are indicated by dashed lines. (c) Matrix of pairwise interaction coefficients determined from a linear additive model, described in the text. The mean and standard deviations as determined from bootstrap sampling are included. (d) The average total bacterial load in each of the di-association combinations, expressed as \log_{10} of total CFUs. The diagonal values are the mono-association load for each of the five species.

There are many ways to quantify interactions from population data. We assume that the log abundance, $\langle \log_{10}(p_i) \rangle$, of a bacterial species, i in the presence of j , grows like,

$$\frac{d \langle \log_{10}(p_i) \rangle}{dt} = r_i f(\langle \log_{10}(p_i) \rangle) \left(1 - \frac{\langle \log_{10}(p_i) \rangle - \sum_{j \neq i} C_{ij} \langle \log_{10}(p_j) \rangle}{\langle \log_{10}(k_i) \rangle} \right), \quad (4.1)$$

where $f(\langle \log_{10}(p_i) \rangle)$ is some function of the log of the bacterial abundance, r_i is the growth rate, k_i is the carrying capacity, N is the number of bacterial species, and C_{ij} are the interaction coefficients. This equation is similar to the competitive Lotka-Volterra equation in which one has uninhibited growth followed by an asymptotic plateau to the bacteria's carrying capacity. However, here we posit that the log of the abundance follows these dynamics instead of the total bacterial abundance. We make this assumption as our bacterial abundances are log-normally distributed as can be seen in Fig 4.1 (d). Importantly, the effects are large enough to shift the abundance by orders of magnitude, so that interactions proportional to log of the population are sensible to assume. Under the assumption that the bacteria have reached steady state, Eq 4.1 becomes,

$$\langle \log_{10}(k_i) \rangle = \langle \log_{10}(p_i) \rangle - \sum_{j \neq i} C_{ij} \langle \log_{10}(p_j) \rangle. \quad (4.2)$$

In the case of only two interacting bacterial species we obtain,

$$\langle \log_{10}(p_i^I) \rangle = \langle \log_{10}(p_i^{II}) \rangle - C_{ij} \langle \log_{10}(p_j^{II}) \rangle. \quad (4.3)$$

The Roman numerals denote the the number of inoculated bacteria; I represents mono-association and II , di-association. Note that we are making the assumption that the mean log carrying capacity for a bacteria is its mean log abundance in mono-association, i.e. $\langle \log_{10}(k_i) \rangle = \langle \log_{10}(p_i^I) \rangle$. Rearranging yields,

$$C_{ij} = \frac{\langle \log_{10}(p_i^{II}) \rangle - \langle \log_{10}(p_i^I) \rangle}{\langle \log_{10}(p_j^{II}) \rangle}, \quad (4.4)$$

from which we can find the pairwise bacterial interaction coefficients, C_{ij} . A negative interaction coefficient means that a bacterial species decreases the

diassociation abundance of another species from that of its mono-associated abundance. In our calculation of the interaction coefficients, we only used data in which both bacterial species were present so as not to include fish in which a particular bacterial species failed to colonize. Fig 4.2 (c) shows these interaction coefficients for each of the bacterial species acting on one another. Bootstrap sampling from the measured sets of bacterial abundances gives the mean and standard deviation of the estimated interaction parameters, C_{ij} , of species j on species i . As expected, AE has no significant interaction coefficients acting on it. AC has several significant positive interactions while EN, PL and to a lesser degree PS have significant negative interactions acting upon them. The load, or total number of bacteria per gut disregarding species type, is similar for all of the di-associations as shown in Fig 4.2 (d).

To see whether these pairwise interactions have predictive power, we consider co-inoculation of all five bacterial species. Examination of over 200 fish shows a large variety of outcomes, depicted in Fig 4.3 (a) as the relative abundance of each species in each larval gut. Multiple species are able to coexist, with the median number of species present being 4, Fig 4.3 (b). The mean total bacterial load as well as its distribution is similar to the mean and distribution of the mono- and di-association experiments, as well as four-species inoculations discussed below, Fig 4.3 (c).

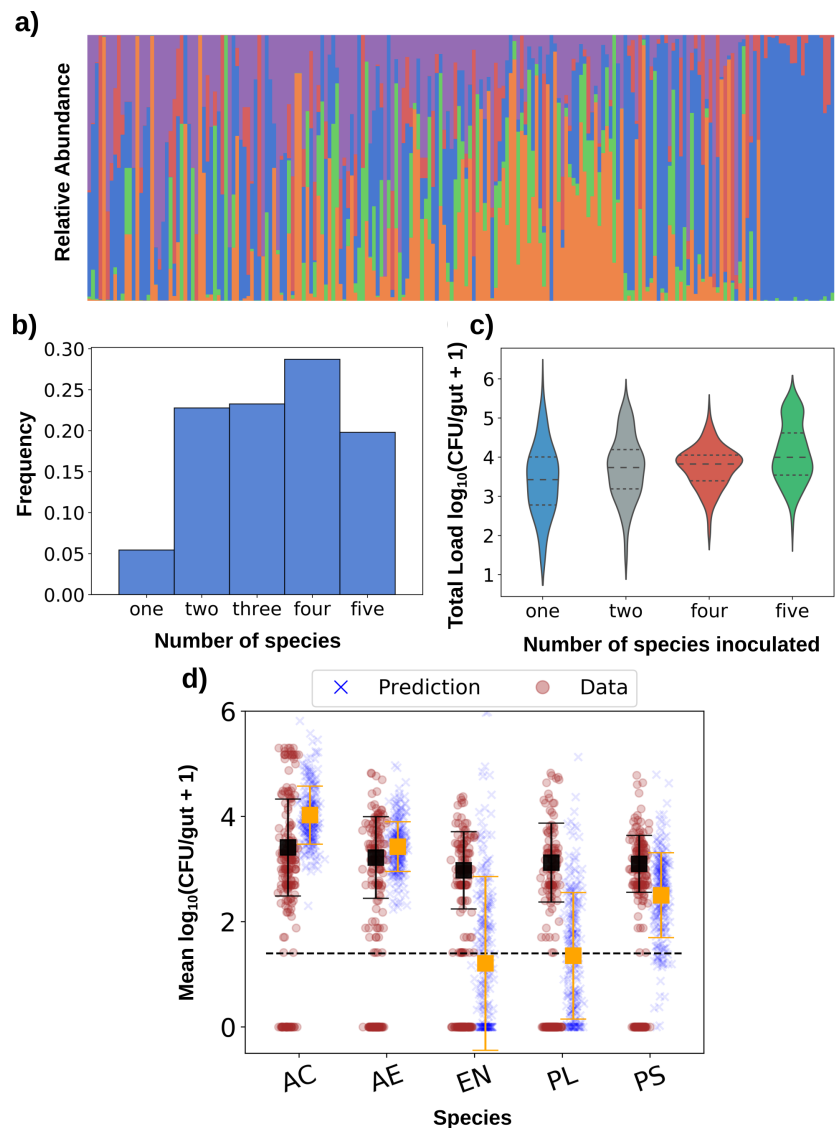


FIGURE 4.3. **Pairwise prediction of the five species community.** (a) Stacked bar plot of the relative abundance of the five bacterial species when all five were co-inoculated. Each bar is a single dissected fish and are ordered by total load. (b) Histogram of the total number of bacterial species from the 5-species inoculations. (c) Violin plots of the total load as a function of total number of inoculated species. (d) Prediction of the abundance of the five different bacterial species from the linear additive model compared to the actual abundance from the 5-species inoculations.

We assess the expected presence and absence of each species, and more precisely the expected numerical abundance of each as determined from the steady

state of Eq. 4.1. The predicted abundance of species i in the presence of species j in the five species case is given by

$$\langle \log_{10} (p_i^I) \rangle = \langle \log_{10} (p_i^V) \rangle - \sum_{j \neq i} C_{ij} \langle \log_{10} (p_j^V) \rangle. \quad (4.5)$$

Rearranging and in matrix form,

$$\langle \log_{10} (\hat{p}_i^V) \rangle = \hat{C}^{-1} \langle \log_{10} (\hat{p}_i^I) \rangle, \quad (4.6)$$

where the roman numeral represents is the number of species present, and \hat{C} is the interaction matrix where $\hat{C}_{ii} = 1$ and the off diagonal elements $\hat{C}_{ij} = -C_{ij}$. We can use Eq. 4.6 with bootstrap sampling to get a prediction of the abundance of each of the five bacterial species when all are co-inoculated and compare to our results from dissection. The predictions as well as the five species data are shown in Fig 4.3 (d). Interestingly, the mean predictions for both EN and PL fall below the detection limit of 25 bacteria per gut as represented by the dashed horizontal line. Thus, in our system, the pairwise interactions fail to predict the abundances in the five species communities. Instead, the strong negative interactions, C_{ij} , from the pairwise inoculations predict near extinction of two of the species that is not seen in the data. Note that the predicted mean abundances for AC, PS and in particular AE are not too far from the means of the data. This failure of prediction suggest that higher order interactions are at play than those calculated using our model.

To further explore the role of pairwise interactions of these bacteria, we can determine the apparent pairwise interactions between species in the 4 and 5 species communities similar to Robert Paine's experiment on the abundance of species commonly found in tide pools [79] in which he explored the effects of removing a

species from a community on other species in that community. In analogy to Eq 4.6, the apparent 4-5 interaction coefficients, \tilde{C}_{ij} , are given by,

$$\tilde{C}_{ij} = \frac{\langle \log_{10}(p_i^V) \rangle - \langle \log_{10}(p_i^{IV}) \rangle}{\langle \log_{10}(p_j^V) \rangle}. \quad (4.7)$$

We performed all five possible different co-inoculations of four bacterial species, and assessed the interaction between species *i* and *j* in this multi-species system by the difference in abundance of species *i* lacking species *j* and in the five-species system as in Eq. 4.7. Thus, we examined all four species communities as well as those four species plus the fifth remaining species in order to see the effects of the fifth species on each of the original four. In our analysis, we only included fish in which all four bacterial species were present which resulted in approximately 11 fish per co-inoculation. As an example, EN abundance in inoculations lacking AC, PL, PS, and AE, as well as its abundance in five-species inoculations, are shown in Fig 4.4 (a). It can be seen that EN does not experience the large abundance change, in either its mean or variance, that we found in the di-association experiments. Again, using bootstrap sampling we determine the mean and standard deviation of the apparent 4-5 interaction coefficients, \tilde{C}_{ij} , which are shown in Fig 4.4 (b). Note that there are no strong negative interaction coefficients in contrast to the pairwise interactions. In fact, the apparent multispecies interactions, \tilde{C}_{ij} , tend to be more positive than their pairwise counterparts, C_{ij} , as shown in Fig 4.4 (c).

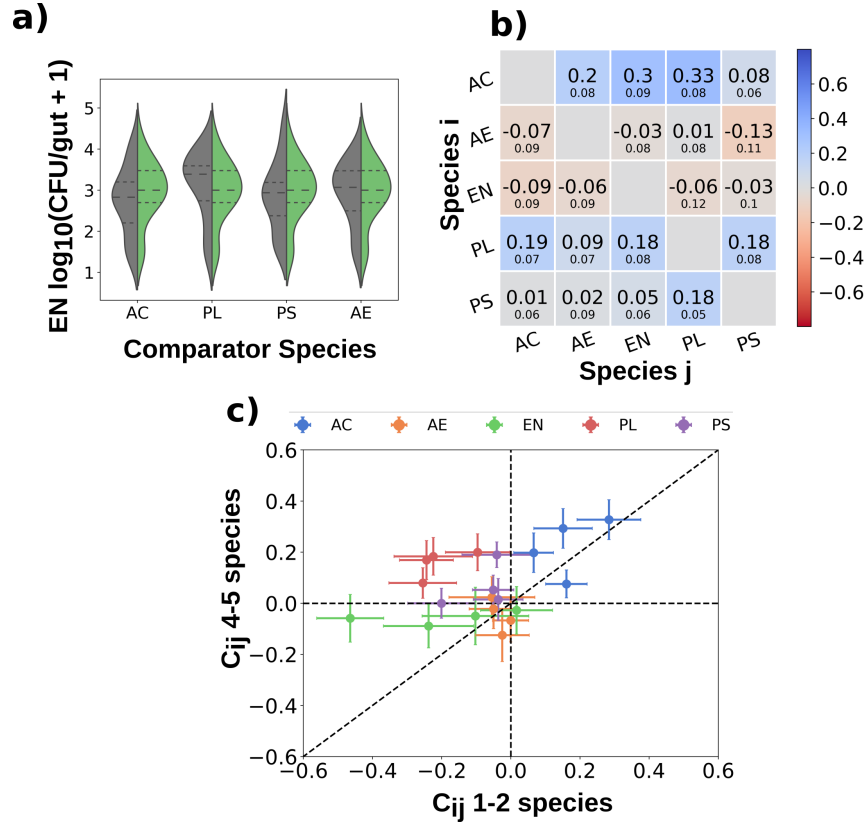


FIGURE 4.4. 4 and 5 bacterial species interactions. (a) violin plot of the total abundance of EN in the 5-species experiment, left side, and each of the 4-species experiments, right side. (b) 4-5 species interaction coefficients. The mean and standard deviation for each coefficient are included as determined from bootstrap sampling. (c) The 4-5 interactions plotted against the 1-2 interactions from Figure 2.

4.4. Conclusions

Our in-vivo study of bacterial interactions using initially germ-free larval zebrafish allows for a controlled, bottom-up approach to probing bacterial interactions in both pairwise inoculated as well as in multi-species communities. We find strong negative interactions between two co-inoculated bacterial species in contrast with more positive interactions in the 4 or 5 species communities. This

could explain why we see a recovery of EN and PL in the five species data when compared to the predictions. Our data imply that higher-order interactions may dampen strong competition between species and therefore foster greater diversity than may be expected from pairwise models. There are many possible causes for this enhanced coexistence, including new metabolic interactions, or partitioning into spatial niches or domains. From earlier work [14] different species in isolation have very different physical organization, and it would be unprecedented to discover alterations of these patterns by co-resident species. To further explore what is driving these higher order interactions our lab plans to study the spatial distribution of these bacteria within the gut. We also plan to complete all ten combinations of 3-species co-inoculations in order to see what apparent 2-3 and 3-4 interactions look like and to see if interaction strength monotonically decreases with number of species.

REFERENCES CITED

- [1] Mitchell L. Sogin, Hilary G. Morrison, Julie A. Huber, David Mark Welch, Susan M. Huse, Phillip R. Neal, Jesus M. Arrieta, and Gerhard J. Herndl. Microbial diversity in the deep sea and the underexplored “rare biosphere”. *Proceedings of the National Academy of Sciences*, 103(32):12115–12120, 2006. ISSN 0027-8424. doi: 10.1073/pnas.0605127103. URL <https://www.pnas.org/content/103/32/12115>.
- [2] R.P. Baker, M.J. Taormina, M. Jemielita, and R. Parthasarathy. A combined light sheet fluorescence and differential interference contrast microscope for live imaging of multicellular specimens. *Journal of Microscopy*, 258(2): 105–112, 2015. doi: 10.1111/jmi.12220. URL <https://onlinelibrary.wiley.com/doi/abs/10.1111/jmi.12220>.
- [3] Philipp J. Keller, Annette D. Schmidt, Joachim Wittbrodt, and Ernst H.K. Stelzer. Reconstruction of zebrafish early embryonic development by scanned light sheet microscopy. *Science*, 322(5904):1065–1069, 2008. ISSN 0036-8075. doi: 10.1126/science.1162493. URL <http://science.sciencemag.org/content/322/5904/1065>.
- [4] Michael Stanton, Michelle Cronin, Panos Lehouritis, and Mark Tangney. In vivo bacterial imaging without engineering; a novel probe-based strategy facilitated by endogenous nitroreductase enzymes. *Current gene therapy*, 15, 01 2015. doi: 10.2174/1566523215666150126122712.
- [5] Michelle Cronin, Ali R. Akin, Sara A. Collins, Jeff Meganck, Jae-Beom Kim, Chwanrow K. Baban, Susan A. Joyce, Gooitzen M. van Dam, Ning Zhang, Douwe van Sinderen, Gerald C. O’Sullivan, Noriyuki Kasahara, Cormac G. Gahan, Kevin P. Francis, and Mark Tangney. High resolution in vivo bioluminescent imaging for the study of bacterial tumour targeting. *PLOS ONE*, 7(1):1–11, 01 2012. doi: 10.1371/journal.pone.0030940. URL <https://doi.org/10.1371/journal.pone.0030940>.
- [6] Matthew Jemielita, Michael J. Taormina, April Delaurier, Charles B. Kimmel, and Raghuveer Parthasarathy. Comparing phototoxicity during the development of a zebrafish craniofacial bone using confocal and light sheet fluorescence microscopy techniques. *Journal of biophotonics*, 6(11-12): 920–928, Dec 2013. ISSN 1864-0648. doi: 10.1002/jbio.201200144. URL <https://www.ncbi.nlm.nih.gov/pubmed/23242824>. 23242824[pmid].

- [7] Jason R. Meyers. Zebrafish: Development of a vertebrate model organism. *Current Protocols Essential Laboratory Techniques*, 16(1):e19, 2018. doi: 10.1002/cpet.19. URL <https://currentprotocols.onlinelibrary.wiley.com/doi/abs/10.1002/cpet.19>.
- [8] Matthew Jemielita, Michael J. Taormina, Adam R. Burns, Jennifer S. Hampton, Annah S. Rolig, Karen Guillemin, and Raghuvveer Parthasarathy. Spatial and temporal features of the growth of a bacterial species colonizing the zebrafish gut. *mBio*, 5(6):e01751–14, Dec 2014. ISSN 2150-7511. doi: 10.1128/mBio.01751-14. URL <http://www.ncbi.nlm.nih.gov/pmc/articles/PMC4271548/>. mBio01751-14[PII].
- [9] W. Zac Stephens, Travis J. Wiles, Emily S. Martinez, Matthew Jemielita, Adam R. Burns, Raghuvveer Parthasarathy, Brendan J. M. Bohannon, and Karen Guillemin. Identification of population bottlenecks and colonization factors during assembly of bacterial communities within the zebrafish intestine. *mBio*, 6(6):e01163–15, Oct 2015. ISSN 2150-7511. doi: 10.1128/mBio.01163-15. URL <http://www.ncbi.nlm.nih.gov/pmc/articles/PMC4626852/>. mBio01163-15[PII].
- [10] W. Zac Stephens, Adam R. Burns, Keaton Stagaman, Sandi Wong, John F. Rawls, Karen Guillemin, and Brendan J. M. Bohannon. The composition of the zebrafish intestinal microbial community varies across development. *ISME J*, 10(3):644–654, Mar 2016. ISSN 1751-7362. doi: 10.1038/ismej.2015.140. URL <http://www.ncbi.nlm.nih.gov/pmc/articles/PMC4817687/>. 26339860[pmid].
- [11] Travis J Wiles, Matthew Jemielita, Ryan P Baker, Brandon H Schlomann, Savannah L Logan, Julia Ganz, Ellie Melancon, Judith S Eisen, Karen Guillemin, and Raghuvveer Parthasarathy. Host gut motility promotes competitive exclusion within a model intestinal microbiota. *PLOS Biology*, 14(7):1–24, 07 2016. doi: 10.1371/journal.pbio.1002517. URL <https://doi.org/10.1371/journal.pbio.1002517>.
- [12] Travis J. Wiles, Elena S. Wall, Brandon H. Schlomann, Edouard A. Hay, Raghuvveer Parthasarathy, and Karen Guillemin. Modernized tools for streamlined genetic manipulation of wild and diverse symbiotic bacteria. *bioRxiv*, 2017. doi: 10.1101/202861. URL <https://www.biorxiv.org/content/early/2017/10/13/202861>.

- [13] Savannah L. Logan, Jacob Thomas, Jinyuan Yan, Ryan P. Baker, Drew S. Shields, Joao B. Xavier, Brian K. Hammer, and Raghuvver Parthasarathy. The vibrio cholerae type vi secretion system can modulate host intestinal mechanics to displace gut bacterial symbionts. *Proceedings of the National Academy of Sciences*, 115(16):E3779–E3787, 2018. ISSN 0027-8424. doi: 10.1073/pnas.1720133115. URL <http://www.pnas.org/content/115/16/E3779>.
- [14] Bacterial cohesion predicts spatial distribution in the larval zebrafish intestine. *Biophysical Journal*, 115(11):2271 – 2277, 2018. ISSN 0006-3495. doi: <https://doi.org/10.1016/j.bpj.2018.10.017>. URL <http://www.sciencedirect.com/science/article/pii/S0006349518311652>.
- [15] RD Allen, GB David, and G. Nomarski. The zeiss-nomarski differential interference equipment for transmitted-light microscopy. *Zeitschrift für wissenschaftliche Mikroskopie und mikroskopische Technik*, 69(4), 1969.
- [16] M Pluta. Advanced light microscopy: Specialized methods. 1989.
- [17] J. Ganz, R. P. Baker, M. K. Hamilton, E. Melancon, P. Diba, J. S. Eisen, and R. Parthasarathy. Image velocimetry and spectral analysis enable quantitative characterization of larval zebrafish gut motility. *Neurogastroenterology & Motility*, 30(9):e13351, 2018. doi: 10.1111/nmo.13351. URL <https://onlinelibrary.wiley.com/doi/abs/10.1111/nmo.13351>.
- [18] Bernard Widrow and Michael A. Lehr. Artificial neural networks of the perceptron, madaline, and backpropagation family. In Hans-Werner BOTHE, Madjid SAMII, and Rolf ECKMILLER, editors, *Neurobionics*, pages 133 – 205. Elsevier, Amsterdam, 1993. ISBN 978-0-444-89958-3. doi: <https://doi.org/10.1016/B978-0-444-89958-3.50013-9>. URL <http://www.sciencedirect.com/science/article/pii/B9780444899583500139>.
- [19] Geoffrey E. Hinton, Simon Osindero, and Yee-Whye Teh. A fast learning algorithm for deep belief nets. *Neural Comput.*, 18(7):1527–1554, July 2006. ISSN 0899-7667. doi: 10.1162/neco.2006.18.7.1527. URL <http://dx.doi.org/10.1162/neco.2006.18.7.1527>.
- [20] Yann Lecun, Lon Bottou, Yoshua Bengio, and Patrick Haffner. Gradient-based learning applied to document recognition. In *Proceedings of the IEEE*, pages 2278–2324, 1998.
- [21] Caroline Cakebread. People will take 1.2 trillion digital photos this year thanks to smartphones. *Business Insider*, Aug 2017.

- [22] Martin Abadi, Paul Barham, Jianmin Chen, Zhifeng Chen, Andy Davis, Jeffrey Dean, Matthieu Devin, Sanjay Ghemawat, Geoffrey Irving, Michael Isard, Manjunath Kudlur, Josh Levenberg, Rajat Monga, Sherry Moore, Derek G. Murray, Benoit Steiner, Paul Tucker, Vijay Vasudevan, Pete Warden, Martin Wicke, Yuan Yu, and Xiaoqiang Zheng. Tensorflow: A system for large-scale machine learning. In *12th USENIX Symposium on Operating Systems Design and Implementation (OSDI 16)*, pages 265–283, 2016. URL <https://www.usenix.org/system/files/conference/osdi16/osdi16-abadi.pdf>.
- [23] F. Pedregosa, G. Varoquaux, A. Gramfort, V. Michel, B. Thirion, O. Grisel, M. Blondel, P. Prettenhofer, R. Weiss, V. Dubourg, J. Vanderplas, A. Passos, D. Cournapeau, M. Brucher, M. Perrot, and E. Duchesnay. Scikit-learn: Machine learning in Python. *Journal of Machine Learning Research*, 12: 2825–2830, 2011.
- [24] Stéfan van der Walt, Johannes L. Schönberger, Juan Nunez-Iglesias, François Boulogne, Joshua D. Warner, Neil Yager, Emmanuelle Gouillart, Tony Yu, and the scikit-image contributors. scikit-image: image processing in Python. *PeerJ*, 2:e453, 6 2014. ISSN 2167-8359. doi: 10.7717/peerj.453. URL <https://doi.org/10.7717/peerj.453>.
- [25] Theano Development Team. Theano: A Python framework for fast computation of mathematical expressions. *arXiv e-prints*, abs/1605.02688, May 2016. URL <http://arxiv.org/abs/1605.02688>.
- [26] François Chollet et al. Keras. <https://github.com/fchollet/keras>, 2015.
- [27] Yangqing Jia, Evan Shelhamer, Jeff Donahue, Sergey Karayev, Jonathan Long, Ross Girshick, Sergio Guadarrama, and Trevor Darrell. Caffe: Convolutional architecture for fast feature embedding. In *Proceedings of the 22Nd ACM International Conference on Multimedia*, MM '14, pages 675–678, New York, NY, USA, 2014. ACM. ISBN 978-1-4503-3063-3. doi: 10.1145/2647868.2654889. URL <http://doi.acm.org/10.1145/2647868.2654889>.
- [28] Ronan Collobert, Koray Kavukcuoglu, and Clément Farabet. Torch7: A matlab-like environment for machine learning. In *BigLearn, NIPS Workshop*, 2011.
- [29] James A. Barnett. Beginnings of microbiology and biochemistry: the contribution of yeast research. *Microbiology*, 149(3):557–567, 2003.
- [30] Charles K. Fisher and Pankaj Mehta. Identifying keystone species in the human gut microbiome from metagenomic timeseries using sparse linear regression. *PLOS ONE*, 9(7):1–10, 07 2014. doi: 10.1371/journal.pone.0102451. URL <https://doi.org/10.1371/journal.pone.0102451>.

- [31] James I. Prosser, Brendan J. M. Bohannon, Tom P. Curtis, Richard J. Ellis, Mary K. Firestone, Rob P. Freckleton, Jessica L. Green, Laura E. Green, Ken Killham, Jack J. Lennon, A. Mark Osborn, Martin Solan, Christopher J. van der Gast, and J. Peter W. Young. The role of ecological theory in microbial ecology. *Nature Reviews Microbiology*, 5:384 EP –, May 2007. URL <https://doi.org/10.1038/nrmicro1643>. Perspective.
- [32] Yandong Xiao, Marco Tulio Angulo, Jonathan Friedman, Matthew K. Waldor, Scott T. Weiss, and Yang-Yu Liu. Mapping the ecological networks of microbial communities. *Nature Communications*, 8(1):2042, 2017. ISSN 2041-1723. doi: 10.1038/s41467-017-02090-2. URL <https://doi.org/10.1038/s41467-017-02090-2>.
- [33] Gerald Burgstaller, Sarah Vierkotten, Michael Lindner, Melanie Knigshoff, and Oliver Eickelberg. Multidimensional immunolabeling and 4d time-lapse imaging of vital ex vivo lung tissue. *American Journal of Physiology-Lung Cellular and Molecular Physiology*, 309(4):L323–L332, 2015. doi: 10.1152/ajplung.00061.2015. URL <https://doi.org/10.1152/ajplung.00061.2015>. PMID: 26092995.
- [34] Roberto Weigert, Natalie Porat-Shliom, and Panomwat Amornphimoltham. Imaging cell biology in live animals: Ready for prime time. *The Journal of Cell Biology*, 201(7):969–979, 2013. ISSN 0021-9525. doi: 10.1083/jcb.201212130. URL <http://jcb.rupress.org/content/201/7/969>.
- [35] Lara Carvalho and Carl-Philipp Heisenberg. *Imaging Zebrafish Embryos by Two-Photon Excitation Time-Lapse Microscopy*, pages 273–287. Humana Press, Totowa, NJ, 2009. ISBN 978-1-60327-977-2. doi: 10.1007/978-1-60327-977-2_17.
- [36] Misha B. Ahrens, Jennifer M. Li, Michael B. Orger, Drew N. Robson, Alexander F. Schier, Florian Engert, and Ruben Portugues. Brain-wide neuronal dynamics during motor adaptation in zebrafish. *Nature*, 485:471 EP –, May 2012. URL <http://dx.doi.org/10.1038/nature11057>. Article.
- [37] Karel Svoboda and Ryohei Yasuda. Principles of two-photon excitation microscopy and its applications to neuroscience. *Neuron*, 50(6):823 – 839, 2006. ISSN 0896-6273. doi: <https://doi.org/10.1016/j.neuron.2006.05.019>. URL <http://www.sciencedirect.com/science/article/pii/S0896627306004119>.
- [38] Philipp J. Keller. Imaging morphogenesis: Technological advances and biological insights. *Science*, 340(6137), 2013. ISSN 0036-8075. doi: 10.1126/science.1234168. URL <http://science.sciencemag.org/content/340/6137/1234168>.

- [39] Philipp J. Keller and Misha B. Ahrens. Visualizing whole-brain activity and development at the single-cell level using light-sheet microscopy. *Neuron*, 85(3):462–483, 2018/02/02 2013. ISSN 0896-6273. doi: 10.1016/j.neuron.2014.12.039. URL <http://dx.doi.org/10.1016/j.neuron.2014.12.039>.
- [40] Alexis Maizel, Daniel von Wangenheim, Fernn Federici, Jim Haseloff, and Ernst H.K. Stelzer. High-resolution live imaging of plant growth in near physiological bright conditions using light sheet fluorescence microscopy. *The Plant Journal*, 68(2):377–385, 2011. ISSN 1365-313X. doi: 10.1111/j.1365-313X.2011.04692.x. URL <http://dx.doi.org/10.1111/j.1365-313X.2011.04692.x>.
- [41] Jan Huisken and Didier Y. R. Stainier. Selective plane illumination microscopy techniques in developmental biology. *Development*, 136(12):1963–1975, 2009. ISSN 0950-1991. doi: 10.1242/dev.022426. URL <http://dev.biologists.org/content/136/12/1963>.
- [42] Periklis Pantazis and Willy Supatto. Advances in whole-embryo imaging: a quantitative transition is underway. *Nature Reviews Molecular Cell Biology*, 15:327 EP –, Apr 2014. URL <http://dx.doi.org/10.1038/nrm3786>. Review Article.
- [43] Alex Krizhevsky, Ilya Sutskever, and Geoffrey E Hinton. Imagenet classification with deep convolutional neural networks. In F. Pereira, C. J. C. Burges, L. Bottou, and K. Q. Weinberger, editors, *Advances in Neural Information Processing Systems 25*, pages 1097–1105. Curran Associates, Inc., 2012.
- [44] Andre Esteva, Brett Kuprel, Roberto A. Novoa, Justin Ko, Susan M. Swetter, Helen M. Blau, and Sebastian Thrun. Dermatologist-level classification of skin cancer with deep neural networks. *Nature*, 542:115 EP –, Jan 2017. URL <http://dx.doi.org/10.1038/nature21056>.
- [45] Matthew D. Zeiler and Rob Fergus. Visualizing and understanding convolutional networks. In David Fleet, Tomas Pajdla, Bernt Schiele, and Tinne Tuytelaars, editors, *Computer Vision – ECCV 2014*, pages 818–833, Cham, 2014. Springer International Publishing.
- [46] S. Kevin Zhou, Hayit Greenspan, and Dinggang Shen. In *Deep Learning for Medical Image Analysis*. Academic Press, 2017. ISBN 978-0-12-810408-8. doi: <https://doi.org/10.1016/B978-0-12-810408-8.00026-2>. URL <https://www.sciencedirect.com/science/article/pii/B9780128104088000262>.

- [47] B. Dong, L. Shao, M. Da Costa, O. Bandmann, and A. F. Frangi. Deep learning for automatic cell detection in wide-field microscopy zebrafish images. In *2015 IEEE 12th International Symposium on Biomedical Imaging (ISBI)*, pages 772–776, April 2015. doi: 10.1109/ISBI.2015.7163986.
- [48] David A. Van Valen, Takamasa Kudo, Keara M. Lane, Derek N. Macklin, Nicolas T. Quach, Mialy M. DeFelice, Inbal Maayan, Yu Tanouchi, Euan A. Ashley, and Markus W. Covert. Deep learning automates the quantitative analysis of individual cells in live-cell imaging experiments. *PLOS Computational Biology*, 12(11):1–24, 11 2016. doi: 10.1371/journal.pcbi.1005177. URL <https://doi.org/10.1371/journal.pcbi.1005177>.
- [49] Ignacio Arganda-Carreras, Verena Kaynig, Curtis Rueden, Kevin W Eliceiri, Johannes Schindelin, Albert Cardona, and H Sebastian Seung. Trainable weka segmentation: a machine learning tool for microscopy pixel classification. *Bioinformatics*, 33(15):2424–2426, 2017. doi: 10.1093/bioinformatics/btx180. URL <http://dx.doi.org/10.1093/bioinformatics/btx180>.
- [50] Feng Ning, D. Delhomme, Y. LeCun, F. Piano, L. Bottou, and P. E. Barbano. Toward automatic phenotyping of developing embryos from videos. *IEEE Transactions on Image Processing*, 14(9):1360–1371, Sept 2005. ISSN 1057-7149. doi: 10.1109/TIP.2005.852470.
- [51] Patrick Ferdinand Christ, Mohamed Ezzeldin A. Elshaer, Florian Ettliger, Sunil Tataavarty, Marc Bickel, Patrick Bilic, Markus Rempfler, Marco Armbruster, Felix Hofmann, Melvin D’Anastasi, Wieland H. Sommer, Seyed-Ahmad Ahmadi, and Bjoern H. Menze. Automatic liver and lesion segmentation in ct using cascaded fully convolutional neural networks and 3d conditional random fields. In Sebastien Ourselin, Leo Joskowicz, Mert R. Sabuncu, Gozde Unal, and William Wells, editors, *Medical Image Computing and Computer-Assisted Intervention – MICCAI 2016*, pages 415–423, Cham, 2016. Springer International Publishing. ISBN 978-3-319-46723-8.
- [52] Oren Z Kraus, Ben T Gryns, Jimmy Ba, Yolanda Chong, Brendan J Frey, Charles Boone, and Brenda J Andrews. Automated analysis of high-content microscopy data with deep learning. *Molecular Systems Biology*, 13(4), 2017. doi: 10.15252/msb.20177551. URL <http://msb.embopress.org/content/13/4/924>.

- [53] Mei Zhan, Matthew M. Crane, Eugeni V. Entchev, Antonio Caballero, Diana Andrea Fernandes de Abreu, QueeLim Chng, and Hang Lu. Automated processing of imaging data through multi-tiered classification of biological structures illustrated using *caenorhabditis elegans*. *PLOS Computational Biology*, 11(4):1–21, 04 2015. doi: 10.1371/journal.pcbi.1004194. URL <https://doi.org/10.1371/journal.pcbi.1004194>.
- [54] Chawin Ounkomol, Sharmishta Seshamani, Mary M. Maleckar, Forrest Collman, and Gregory R. Johnson. Label-free prediction of three-dimensional fluorescence images from transmitted-light microscopy. *Nature Methods*, 2018. ISSN 1548-7105. doi: 10.1038/s41592-018-0111-2. URL <https://doi.org/10.1038/s41592-018-0111-2>.
- [55] H. Shin, H. R. Roth, M. Gao, L. Lu, Z. Xu, I. Nogues, J. Yao, D. Mollura, and R. M. Summers. Deep convolutional neural networks for computer-aided detection: Cnn architectures, dataset characteristics and transfer learning. *IEEE Transactions on Medical Imaging*, 35(5):1285–1298, May 2016. ISSN 0278-0062. doi: 10.1109/TMI.2016.2528162.
- [56] X. Wang, Y. Peng, L. Lu, Z. Lu, M. Bagheri, and R. M. Summers. Chestx-ray8: Hospital-scale chest x-ray database and benchmarks on weakly-supervised classification and localization of common thorax diseases. In *2017 IEEE Conference on Computer Vision and Pattern Recognition (CVPR)*, pages 3462–3471, July 2017. doi: 10.1109/CVPR.2017.369.
- [57] Ali Madani, Ramy Arnaout, Mohammad Mofrad, and Rima Arnaout. Fast and accurate view classification of echocardiograms using deep learning. *npj Digital Medicine*, 1(1):6, 2018. ISSN 2398-6352. doi: 10.1038/s41746-017-0013-1. URL <https://doi.org/10.1038/s41746-017-0013-1>.
- [58] Claire Lifan Chen, Ata Mahjoubfar, Li-Chia Tai, Ian K. Blaby, Allen Huang, Kayvan Reza Niazi, and Bahram Jalali. Deep learning in label-free cell classification. *Scientific Reports*, 6:21471 EP –, Mar 2016. URL <http://dx.doi.org/10.1038/srep21471>. Article.
- [59] Michael J. Taormina, Edouard A. Hay, and Raghuveer Parthasarathy. Passive and active microrheology of the intestinal fluid of the larval zebrafish. *Biophysical Journal*, 113(4):957 – 965, 2017. ISSN 0006-3495. doi: <https://doi.org/10.1016/j.bpj.2017.06.069>. URL <http://www.sciencedirect.com/science/article/pii/S000634951730797X>.

- [60] Alexander Mathis, Pranav Mamidanna, Kevin M. Cury, Taiga Abe, Venkatesh N. Murthy, Mackenzie Weygandt Mathis, and Matthias Bethge. Deeplabcut: markerless pose estimation of user-defined body parts with deep learning. *Nature Neuroscience*, 21(9):1281–1289, 2018. ISSN 1546-1726. doi: 10.1038/s41593-018-0209-y. URL <https://doi.org/10.1038/s41593-018-0209-y>.
- [61] Kathryn Milligan-Myhre, Jeremy R. Charette, Ryan T. Phennicie, W. Zac Stephens, John F. Rawls, Karen Guillemin, and Carol H. Kim. Chapter 4 - study of hostmicrobe interactions in zebrafish. In H. William Detrich, Monte Westerfield, and Leonard I. Zon, editors, *The Zebrafish: Disease Models and Chemical Screens*, volume 105 of *Methods in Cell Biology*, pages 87 – 116. Academic Press, 2011. doi: <https://doi.org/10.1016/B978-0-12-381320-6.00004-7>. URL <http://www.sciencedirect.com/science/article/pii/B9780123813206000047>.
- [62] Jason Yosinski, Jeff Clune, Yoshua Bengio, and Hod Lipson. How transferable are features in deep neural networks? In *Proceedings of the 27th International Conference on Neural Information Processing Systems - Volume 2*, NIPS’14, pages 3320–3328, Cambridge, MA, USA, 2014. MIT Press. URL <http://dl.acm.org/citation.cfm?id=2969033.2969197>.
- [63] Jeff Donahue, Yangqing Jia, Oriol Vinyals, Judy Hoffman, Ning Zhang, Eric Tzeng, and Trevor Darrell. Decaf: A deep convolutional activation feature for generic visual recognition. In Eric P. Xing and Tony Jebara, editors, *Proceedings of the 31st International Conference on Machine Learning*, volume 32 of *Proceedings of Machine Learning Research*, pages 647–655, Beijing, China, 22–24 Jun 2014. PMLR. URL <http://proceedings.mlr.press/v32/donahue14.html>.
- [64] Michael J. Taormina, Matthew Jemielita, W. Zac Stephens, Adam R. Burns, Joshua V. Troll, Raghuv eer Parthasarathy, and Karen Guillemin. Investigating bacterial-animal symbioses with light sheet microscopy. *The Biological Bulletin*, 223(1):7–20, 2012. doi: 10.1086/BBLv223n1p7. URL <https://doi.org/10.1086/BBLv223n1p7>. PMID: 22983029.
- [65] Dan Cirosan, Alessandro Giusti, Luca M. Gambardella, and Jürgen Schmidhuber. Deep neural networks segment neuronal membranes in electron microscopy images. In F. Pereira, C. J. C. Burges, L. Bottou, and K. Q. Weinberger, editors, *Advances in Neural Information Processing Systems 25*, pages 2843–2851. Curran Associates, Inc., 2012.

- [66] Olaf Ronneberger, Philipp Fischer, and Thomas Brox. U-net: Convolutional networks for biomedical image segmentation. *CoRR*, abs/1505.04597, 2015. URL <http://dblp.uni-trier.de/db/journals/corr/corr1505.html>RonnebergerFB15.
- [67] Segmentation of neuronal structures in em stacks challenge - isbi 2012. URL http://brainiac2.mit.edu/isbi_challenge/home.
- [68] J. Long, E. Shelhamer, and T. Darrell. Fully convolutional networks for semantic segmentation. In *2015 IEEE Conference on Computer Vision and Pattern Recognition (CVPR)*, pages 3431–3440, June 2015. doi: 10.1109/CVPR.2015.7298965.
- [69] Marc-Emmanuel Dumas, Richard H. Barton, Ayo Toyé, Olivier Cloarec, Christine Blancher, Alice Rothwell, Jane Fearnside, Roger Tatoud, Véronique Blanc, John C. Lindon, Steve C. Mitchell, Elaine Holmes, Mark I. McCarthy, James Scott, Dominique Gauguier, and Jeremy K. Nicholson. Metabolic profiling reveals a contribution of gut microbiota to fatty liver phenotype in insulin-resistant mice. *Proceedings of the National Academy of Sciences*, 103(33):12511–12516, 2006. ISSN 0027-8424. doi: 10.1073/pnas.0601056103. URL <https://www.pnas.org/content/103/33/12511>.
- [70] Wendy S. Garrett, Graham M. Lord, Shivesh Punit, Geanncarlo Lugo-Villarino, Sarkis K. Mazmanian, Susumu Ito, Jonathan N. Glickman, and Laurie H. Glimcher. Communicable ulcerative colitis induced by t-bet deficiency in the innate immune system. *Cell*, 131(1):33 – 45, 2007. ISSN 0092-8674. doi: <https://doi.org/10.1016/j.cell.2007.08.017>. URL <http://www.sciencedirect.com/science/article/pii/S009286740701080X>.
- [71] Jennifer Hampton Hill, Eric A Franzosa, Curtis Huttenhower, and Karen Guillemin. A conserved bacterial protein induces pancreatic beta cell expansion during zebrafish development. *eLife*, 5:e20145, dec 2016. ISSN 2050-084X. doi: 10.7554/eLife.20145. URL <https://doi.org/10.7554/eLife.20145>.
- [72] Jing Yan, Jeremy W. Herzog, Kelly Tsang, Caitlin A. Brennan, Maureen A. Bower, Wendy S. Garrett, Balfour R. Sartor, Antonios O. Aliprantis, and Julia F. Charles. Gut microbiota induce igf-1 and promote bone formation and growth. *Proceedings of the National Academy of Sciences*, 113(47): E7554–E7563, 2016. ISSN 0027-8424. doi: 10.1073/pnas.1607235113. URL <https://www.pnas.org/content/113/47/E7554>.
- [73] Lora V. Hooper, Dan R. Littman, and Andrew J. Macpherson. Interactions between the microbiota and the immune system. *Science*, 336(6086): 1268–1273, 2012. ISSN 0036-8075. doi: 10.1126/science.1223490. URL <https://science.sciencemag.org/content/336/6086/1268>.

- [74] Niv Zmora, Gili Zilberman-Schapira, Jotham Suez, Uria Mor, Mally Dori-Bachash, Stavros Bashiardes, Eran Kotler, Maya Zur, Dana Regev-Lehavi, Rotem Ben-Zeev Brik, Sara Federici, Yotam Cohen, Raquel Linevsky, Daphna Rothschild, Andreas E. Moor, Shani Ben-Moshe, Alon Harmelin, Shalev Itzkovitz, Nitsan Maharshak, Oren Shibolet, Hagit Shapiro, Meirav Pevsner-Fischer, Itai Sharon, Zamir Halpern, Eran Segal, and Eran Elinav. Personalized gut mucosal colonization resistance to empiric probiotics is associated with unique host and microbiome features. *Cell*, 174(6): 1388–1405.e21, Sep 2018. ISSN 0092-8674. doi: 10.1016/j.cell.2018.08.041. URL <https://doi.org/10.1016/j.cell.2018.08.041>.
- [75] Anthony Ortiz Lopez, Nicole M Vega, and Jeff Gore. Interspecies bacterial competition determines community assembly in the *c. elegans* intestine. *bioRxiv*, 2019. doi: 10.1101/535633. URL <https://www.biorxiv.org/content/early/2019/01/30/535633>.
- [76] Alison L. Gould, Vivian Zhang, Lisa Lamberti, Eric W. Jones, Benjamin Obadia, Nikolaos Korasidis, Alex Gavryushkin, Jean M. Carlson, Niko Beerenwinkel, and William B. Ludington. Microbiome interactions shape host fitness. *Proceedings of the National Academy of Sciences*, 115(51): E11951–E11960, 2018. ISSN 0027-8424. doi: 10.1073/pnas.1809349115. URL <https://www.pnas.org/content/115/51/E11951>.
- [77] Andrés Aranda-Díaz, Benjamin Obadia, Tani Thomsen, Zachary F. Hallberg, Zehra Tüzün Güvener, Kerwyn Casey Huang, and William B. Ludington. Bacterial interspecies interactions modulate ph-mediated antibiotic tolerance in a model gut microbiota. *bioRxiv*, 2019. doi: 10.1101/538132. URL <https://www.biorxiv.org/content/early/2019/03/09/538132>.
- [78] E. Melancon, S. Gomez De La Torre Canny, S. Sichel, M. Kelly, T. J. Wiles, J. F. Rawls, J. S. Eisen, and K. Guillemin. Best practices for germ-free derivation and gnotobiotic zebrafish husbandry. *Methods in cell biology*, 138: 61–100, 2017. ISSN 0091-679X. doi: 10.1016/bs.mcb.2016.11.005. URL <https://www.ncbi.nlm.nih.gov/pubmed/28129860>. 28129860[pmid].
- [79] R. T. Paine. Food webs: Linkage, interaction strength and community infrastructure. 49(3):667–685, 1980. doi: 10.2307/4220. URL <http://www.jstor.org/stable/4220>.